Numerical Simulation of an Intense Squall Line during 10–11 June 1985 PRE-STORM. Part I: Model Verification

DA-LIN ZHANG,* KUN GAO** AND DAVID B. PARSONS

National Center for Atmospheric Research,† Boulder, Colorado

(Manuscript received 19 July 1988, in final form 23 November 1988)

ABSTRACT

A 24-h nested-grid simulation of an intense squall line during the 1985 PRE-STORM experiment is presented using an improved version of the Pennsylvania State University/National Center for Atmospheric Research three-dimensional mesoscale model. Although the model is initialized at 1200 UTC 10 June 1985 with *conventional meteorological observations*, it reproduces remarkably well many observed meso-β scale features that are analyzed from the high-resolution network data. These include 1) the generation of two areas of deep convection at the model initial time; 2) the timing of the initiation of the squall line along a surface front 9 h into the model integration; 3) the development of several convective bands at 2100 UTC; 4) the rapid intensification and rapid dissipation processes of the squall line as it entered and moved out of the network, respectively; 5) the generation of a presquall mesolow, a squall-induced mesohigh and a wake low as well as corresponding multiple surface convergence–divergence flow structure; 6) the evolution of a traveling 700 mb shortwave; 7) the development of a rear-inflow jet; 8) the leading convective rainfall followed by a transition zone and trailing stratiform precipitation; 9) the observed configuration of front-to-rear relative flow at both upper and lower levels separated by the rear-to-front flow at midlevels; 10) the simulation of "onion-shaped" soundings; 11) the splitting of the wake low; 12) the maintenance and intensification of a mesovortex; 13) the distribution and magnitude of convective and stratiform rainfall; and 14) the diurnal cycle of the planetary boundary layer.

One of the encouraging results is that the model accurately simulates the rear-inflow jet as verified against Doppler windprofiler data after the 18-h integration from essentially synoptic-scale initial conditions. The results confirm the previously proposed hypothesis that the wake low develops hydrostatically as a consequence of adiabatic warming by descending flow entering the squall line within the rear-inflow jet. The observed "onion-shaped" soundings are a manifestation of the warming and drying of air within the descending rear inflow jet. It is found that the present wake low is not a transient meso-β scale phenomenon, but has a time scale of more than 50% of the squall line lifetime. Another finding is that the present mesovortex is not produced by latent heat release associated with the squall line but was in existence prior to the model initialization time. The vortex appears to have a significant effect on the distribution of the rainfall associated with the squall line and on the intensity of the rear-inflow jet. Other mesoscale circulation features are also documented in this paper.

This study, along with previous investigations using the model, indicates that the meso-β scale structure and evolution of MCSs under certain synoptic-scale environmental conditions can be well simulated using the standard network observations if compatible grid resolution, reasonable model physics and initial conditions are utilized.

1. Introduction

Squall lines are frequently observed during the warm season over many parts of the world. Together with another type of the warm-season mesoscale convective system (MCS), termed by Maddox (1980) the mesoscale convective complex (MCC), they have been found to account for a large portion of annual rainfall over the central and eastern United States (e.g., Fritsch et al. 1981; Heideman and Fritsch 1988) and severe weather events (Newton 1967) during spring and summer seasons. Since these two types of MCSs occur on a scale too small to be resolved by the standard rawinsonde network or handled by operational numerical weather prediction models, the progress in the warm-season quantitative precipitation forecasts (QPFs) and severe weather forecasts has been slow, particularly as compared with cold-season events (Ramage 1982; Geogakakos and Hudlow 1984). Hence, several field experiments in diverse geographic regions have been recently carried out to meet the growing concern and interest in improving our understanding and skill in forecasts and warnings of those events.

The present study focuses on a numerical investigation of an intense squall line that was observed to

* Present affiliation: Department of Physics, University of Toronto, Toronto, Ontario, Canada.

** On leave from Department of Geography, Hang-zhou University, People's Republic of China.

† The National Center for Atmospheric Research (NCAR) is funded by the National Science Foundation.

Corresponding author address: Dr. Da-Lin Zhang, Dept. of Physics, University of Toronto, Toronto, Ontario, Canada M5S 1A7.

produce a devastating tornado, hail and severe wind gusts during 10–11 June 1985 PRE-STORM (Preliminary Regional Experiment for STORM–Central, see Cunning 1986). This study represents a continuing research effort, following Zhang and Fritsch (1986, 1988b), to demonstrate that *the meso-β scale structure and evolution of MCSs can be numerically simulated from conventional meteorological observations if compatible grid resolution, reasonable model physics and initial conditions are utilized,* and to provide *much needed understanding of the dynamics of MCSs.* In addition, the observational PRE-STORM network, which provided supplemental rawinsondes, surface reports, conventional and Doppler radars, acoustic sounders, profilers and research aircraft, allows for a more stringent test of the model's capability in reproducing observed mesoscale events. The dynamically consistent four-dimensional high-resolution model results may in turn provide further insight into the dynamic structure and evolution of the MCS.

Squall lines have been extensively studied for many years both observationally (e.g., Newton 1950, 1967; Ogura and Liou 1980; Smull and Houze 1985) and numerically (e.g., Moncrieff and Miller 1976; Chang et al. 1981; Ross 1987). Some common characteristics have emerged from these studies. These include upshear tilt of updrafts, inflow of high-θ_e air near the leading edge of the gust front, midlevel rear inflow of low-θ_e air, gravitational descending of midlevel convective-scale low-θ_e air and trailing stratiform rainfall. The 10–11 June squall line exhibits many of these classic characteristics. In addition, the PRE-STORM dataset permits perhaps the most detailed examination of a squall line that has existed to date. Thus, this case has received a great deal of attention in observational studies. For instance, Augustine and Zipser (1987) used Doppler radar wind profilers to document strong backing winds with height capped by a midlevel rear-inflow jet with a maximum wind of 30 m s^{-1} behind the squall line and low-level veering-wind profiles ahead of the line. Cunning and Blanchard (1987) examined the interactions and feedbacks between the various scales of motion in the evolution of the squall system. Vasiloff and Bluestein (1988) studied the radar reflectivity and Doppler velocity structure during the transition between the mature and dissipative phases.

Rutledge and MacGorman (1988) investigated lightning characteristics associated with peak convective and *stratiform*[1] rainfall during the development stage of the squall system. Based on radar analysis, Rutledge et al. (1988), hereafter referred to as R88, showed that mesoscale updrafts and downdrafts similar to tropical MCSs are present in this squall system, and found that the mesoscale downdrafts initiate at the top of the sloped rear-inflow jet and are closely related to the intensity of the jet.

Using the PRE-STORM network data, Johnson and Hamilton (1988, hereafter referred to as JH88) analyzed three well-known but not well-understood pressure signatures associated with the squall line: a presquall mesolow, a squall-induced mesohigh and a wake low. They found that the wake low, which occurred at the back edge of the surface stratiform rainfall, appears to correspond to the location of the descending rear-inflow jet. The observed "onion-shaped" soundings seem to be the result of warming and drying occurring within the descending rear-inflow jet. JH88 also found a significant contribution (30%–40%) of stratiform rainfall to total squall precipitation. Meanwhile, they noted a mesovortex circulation within the stratiform region. The correlation of significant stratiform rainfall to the presence of the mesovortex has also been observed in other case studies such as Houze (1977), Leary and Rappaport (1987) and Zhang and Fritsch (1987).

This study is the first in a series of papers that numerically investigate how the 10–11 June squall system developed, produced surface presquall mesolows, mesohighs and wake lows, and how the rear-inflow jet forms and affects the development of deep convection and stratiform rain. The objective of this paper is to present verification of a 24-h nested-grid simulation (i.e., from 1200 UTC 10 to 1200 UTC 11 June) of the squall system *using the standard upper-air and surface observations* in order to establish enough credibility for the results of diagnostic computations and scientific experiments to be presented in subsequent parts of this series of papers. Another objective of this paper is to thoroughly document the evolution of the squall system from its prestorm conditions 9 h before its onset to its dissipation. Section 2 describes the major features of the model simulation system. Section 3 discusses prestorm larger-scale environmental conditions at the model initial time. Section 4 compares the model simulation with the previously mentioned observational studies and other available data, and describes the mechanisms whereby the squall line develops and decays. A summary and concluding remarks are given in the final section.

2. Model simulation system

The model used for this study is an improved version of the Pennsylvania State University/National Center for Atmospheric Research (PSU/NCAR) three-dimensional mesoscale hydrostatic model described by Anthes and Warner (1978) and Anthes et al. (1987); it is similar to the version used by Zhang and Fritsch (1986), Zhang et al. (1988) and Zhang (1989) for the 1977 Johnstown flood events, and Zhang and Fritsch

[1] The term stratiform is used rather loosely here since Leary and Rappaport (1987) have shown that stratiform regions are sometimes marginally convective. A more appropriate term from the modeling standpoint is "resolvable-scale" or "explicit" rainfall.

(1988b) for an Oklahoma MCC study. We consider the following model features are important for the present case study:

- a two-way interactive nested-grid procedure which allows incorporation of realistic terrain (Zhang et al. 1986); the model topography is obtained from NCAR 30-min resolution terrain tape using a Cressman-type objective analysis technique (see Fig. 1 for the distribution of the fine-mesh terrain).
- an improved implicit convective scheme of Fritsch–Chappell (1980; Zhang and Fritsch 1986) for the fine mesh and Anthes–H. L. Kuo (Anthes et al. 1987) for the coarse-mesh portion of the nested-grid model;
- an explicit convective scheme containing predictive equations for cloud water (ice) and rainwater (snow), which follows Hsie et al. (1984), Lin et al. (1983) and Rutledge and Hobbs (1983); in this scheme, the effects of hydrostatic water loading, condensation and evaporation, freezing and melting, and deposition/sublimation processes have all been incorporated (see Zhang 1989, for a detailed description).
- a modified version of the Blackadar "large-eddy exchange" high-resolution planetary boundary layer (PBL) parameterization (Zhang and Anthes 1982; Zhang and Fritsch 1986). In this PBL package, the ground temperature is predicted using the surface energy budget in which the effects of short- and longwave radiation and model-predicted cloud cover are included (Benjamin and Carlson 1986; Zhang and Fristch 1986).

The nested-grid ratio is 1:3 with a fine-mesh length of 25 km and a coarse-mesh length of 75 km. The number of grid points for (x, y, σ) dimensions of the coarse and fine meshes are $49 \times 41 \times 19$ and $61 \times 49 \times 19$, respectively. The vertical terrain-following coordinate, σ, is defined as $\sigma = (p - p_t)/(p_s - p_t)$ where p_t is the pressure at the top of the model atmosphere (in this case 80 mb) and p_s is the surface pressure. The 19 computational σ levels are 0.9985, 0.977, 0.929, 0.873, 0.817, 0.761, 0.7045, 0.6475, 0.5705, 0.535, 0.4705, 0.41, 0.3505, 0.272, 0.2345, 0.178, 0.125, 0.075 and 0.025, which are identical to those used by Zhang and Fritsch (1986, 1988b). Figure 1 shows the model domain of both fine and coarse meshes for this study. The PRE-STORM region is selected as a subarea of the fine-mesh domain in which the model simulation will be extensively verified against all available high-resolution observations. This verification region is purposely located near the eastern interface of the nested-grid mesh, since the upstream grid resolution is considered to be essential in helping generate smaller-scale features that subsequently propagate downstream. This has been confirmed by Seaman et al. (1988). In the present case, a shallow surface cold front was propagating into the network area during the first nine model hours and is responsible for the later initiation

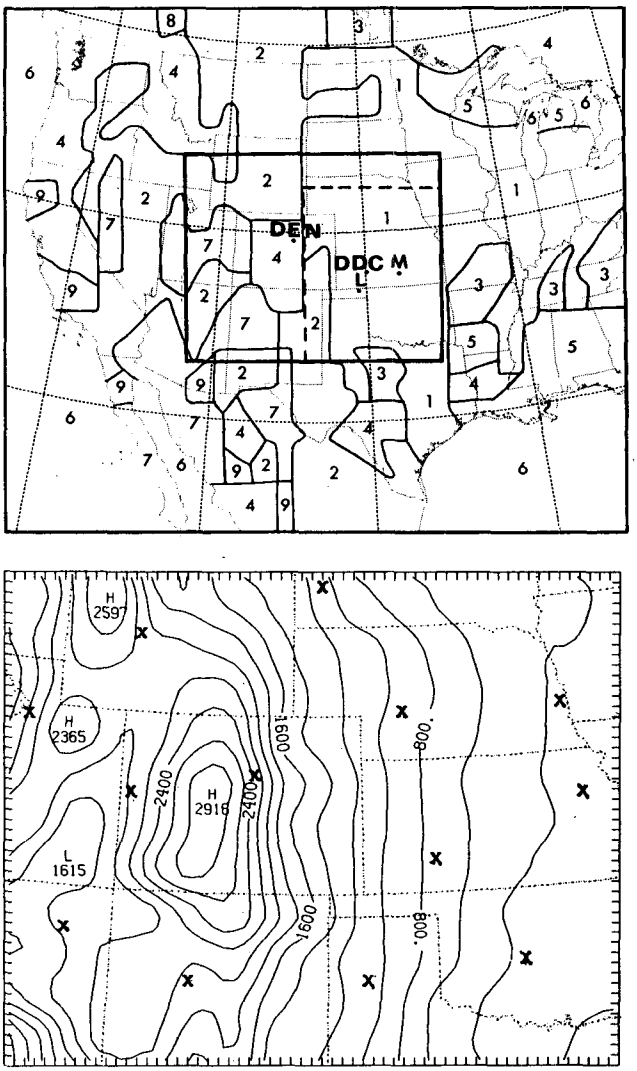

FIG. 1. (a) The nested-grid domain with surface index distribution. Table 1 provides the value for the surface index. The interior thick solid lines denote the mesh interface and the dashed lines indicate the sub-domain used for the presentation of the fine-mesh simulation. (b) The terrain distribution over the fine-mesh domain. Symbol 'x' denotes the location of the standard rawinsonde sites for 1200 UTC 10 June 1985. The intervals marked on the frame are mesh grids (25 km for fine mesh and 75 km for coarse mesh, similarly in the rest of figures).

of the squall line. Hence, such a fine-mesh configuration would allow the model to generate more realistic intense gradients associated with the frontal system and prestorm environment prior to the onset of the squall line.

The implicit and explicit convective schemes are operating simultaneously to account for the separate effects of subgrid-scale deep convection and resolvable-scale phase changes (see Zhang et al. 1988 for a detailed description). The implicit convective scheme and the Blackadar boundary-layer parameterization are basi-

cally the same as that used in previous simulations of the 1977 Johnstown MCSs (Zhang and Fritsch 1986) and an Oklahoma MCC event (Zhang and Fritsch 1988b). The geographic distribution of surface parameters (e.g., moisture availability, roughness length, albedo, thermal capacity and emissivity) which determine surface energy budgets and the development of the PBL, is derived from the land-use data archived at NCAR. A surface index describing these parameters is assigned to each grid point (see Fig. 1a); this is accomplished with the use of a look-up table (see Table 1). The explicit convective scheme is identical to that used by Zhang (1989) and Zhang and Fritsch (1988b) except that terminal velocities of raindrops and snow are subjectively reduced by 70%. We consider that this procedure is a necessary step towards obtaining a satisfactory simulation, since it was found during initial experimental simulations that the inclusion of hydrostatic water loading, evaporation and melting greatly retarded but could not totally prevent the development of CISK-like instability (see Zhang et al. 1988 for a detailed discussion). The resulting upward motion is as strong as 5–6 m s^{-1} on the 25 km grid scale, and thus, as expected, leads to localized excessive rainfall (Molinari and Dudek 1986; Kalb 1987; Zhang et al. 1988). As shown in Zhang (1989), original formulae for computing the terminal velocity are adapted from non-hydrostatic cloud models using a grid resolution much less than 5 km (e.g., see Lin et al. 1983). Therefore, when they are applied to the present model with the grid increment of 25 km, the fallspeed is clearly too large to account for the effect of hydrostatic water loading in nature. The reduction of fallspeeds by 70% is based upon the evaluation of general updraft strength in a cloud model ($\approx$15–20 m s^{-1}) and the maximum upward motion in the present model simulation.

The nested-grid model is initialized at 1200 UTC 10 June 1985 using the technique described by Zhang et al. (1986). Briefly, the procedure begins by interpolating operational analysis from the National Meteorological Center (NMC) global 2.5° latitude–longitude grid to the coarse mesh of the model domain as a first guess. The NMC analysis includes horizontal winds, temperature, relative humidity at all mandatory pressure levels, and sea-level pressure, surface and sea-level temperatures. These fields are then vertically interpolated to the following significant pressure levels: 950, 900, 800 and 600 mb. All these "first guess" fields at both mandatory and significant levels are then enhanced with the standard rawinsonde station soundings using a successive-correction type of objective-analysis technique (Benjamin and Seaman 1985). The fine mesh is initialized similarly except that the enhanced coarse-mesh-interpolated values are utilized as a first guess. No balancing between mass and wind fields is performed; however, the vertically integrated divergence in a column is removed from the wind field to minimize noise early in the model integration. The time-dependent outermost coarse-mesh lateral boundary conditions are obtained by interpolating the 12-h observational analyses linearly in time and specifying them according to Perkey and Kreitzberg (1976). For a more detailed description of the different aspects of the PSU/NCAR model simulation system, the reader is referred to Zhang and Fritsch (1986), Anthes et al. (1987) and Zhang (1989).

Note that the PRE-STORM network did not collect supplementary data until 2100 UTC 10 June when the squall line developed and began to move into the network area. There were also no subjectively constructed upper-air soundings employed for preprocessing the initial data. Thus, this numerical case study first faces a serious challenge, namely, can the model reproduce the development of deep convection at nearly the right time and location after more than nine hours of the model integration and with the conventional-data produced initial conditions? (Fig. 1b shows the distribution of the standard rawinsonde stations over the fine-mesh domain.) The second challenge is, of course, whether or not the model dynamic system can properly repro-

TABLE 1. Description of landuse index and surface parameters (adapted from Anthes et al. 1987).

Surface index	Landuse description	Moisture availability (%)	Roughness length (m)	Albedo (%)	Thermal capacity ($\times 10^5$ J m^{-2} k^{-1})	Emissivity (%)
1	Agriculture	30	0.15	17	1.3	92
2	Range–grassland	15	0.12	19	1.0	92
3	Deciduous forest	30	0.50	16	1.3	93
4	Coniferous forest	30	0.50	12	1.3	95
5	Mixed forest and wet land	35	0.40	14	1.6	95
6	Water	100	0.0001[@]	8	2.0	98
7	Desert	2	0.10	25	0.7	85
8	Tundra	50	0.10	15	1.6	92
9	Savannah	15	0.15	20	1.0	92

[@] This is a background value (z_{0b}) used in the calculation of roughness length over water surface; $z_0 = 0.032u_*^2/g + z_{0b}$ (see Delsol et al. 1971), where u_* is the friction velocity and g is the gravity.

duce the observed internal meso-β scale features associated with the squall system from the initial synoptic-scale data.

3. Initial environmental conditions

The large-scale environmental conditions at the model initial time (i.e., 1200 UTC 10 June 1985) are outlined in Figs. 2–5. In Fig. 2, of major interest is a cold front which has two arc-shaped segments over the northern (termed *sector A*) and northwestern (termed *sector B*) portions of the fine-mesh domain. The major squall line was observed to initiate along the sector *A* cold front around 1930 UTC 10 June and enter the PRE-STORM network at 2100 UTC. Behind the cold front, there is a suggestion of two air streams with northerly and northwesterly flow (denoted by bold streamlines in Fig. 2b) that is highly baroclinic with a strong cross-isobaric component. The flow over the northern half of the domain is more or less characterized by a cyclonic rotation since, as will be discussed in the next section, a mesovortex was initially located near the Nebraska–Wyoming border. Above the surface (see Fig. 4), significant thermal contrast up to 500 mb occurs near the front with the cold air mass impinging on the western slopes of the Rocky Mountains. At 700 mb (Fig. 3), there is a short-wave trough accompanying the surface front with considerable northwesterly cold advection to the rear of the trough axis. Since the temperature ridge coincided with the trough of geopotential heights, the amplitude of the short-wave decreases with height (e.g., see 500 mb analysis in Fig. 3). Near the advancing edge of the cold front (Fig. 4), a moist air mass in the midtroposphere attends the short-wave trough with a very dry air mass below (see Fig. 3 and Denver sounding in Fig. 5). This moist air mass appears to correspond to the already developed convective clouds along the front (see Fig. 6). The juxtaposition of the deep cool pool with the strong cold advection behind the cold front and short-wave trough could clearly assist the cold frontogenesis, and later southeastward acceleration of the front after passing over the mountain peak.

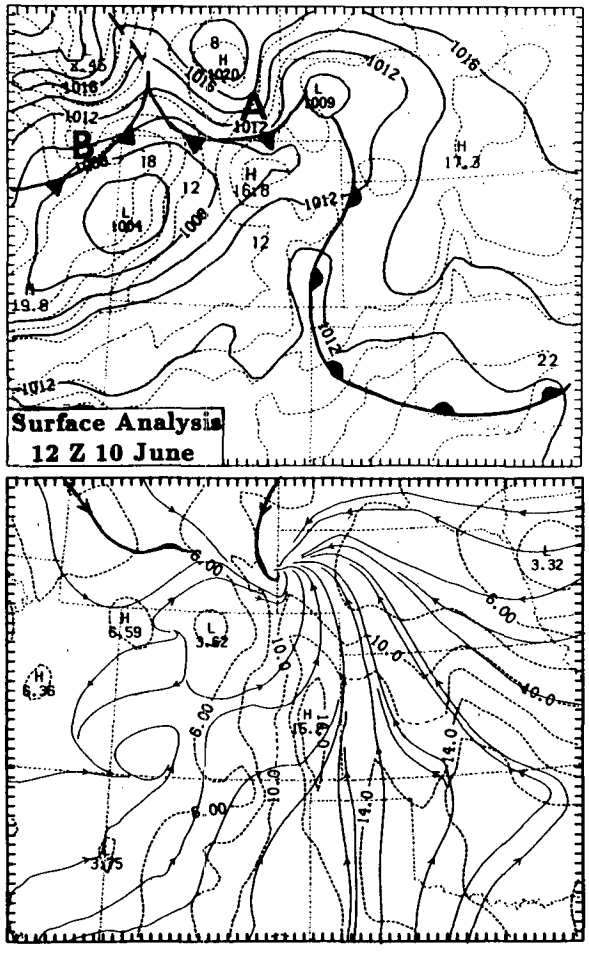

FIG. 2. Surface synoptic analysis over the fine-mesh domain for 1200 UTC 10 June 1985. (a) Sea-level pressure at intervals of 2 mb (solid lines), and temperature at intervals of 2°C (dashed lines). Letters "*A*" and "*B*" denote two segments of the surface front (see text). (b) Stream line (solid lines), and specific humidity (dashed lines) at intervals of 2 g kg^{-1}.

Ahead of this advancing cold front southeastward, there is a quasi-stationary warm front positioned to the west and south of the network area (see Fig. 2). Associated with the warm front is a southerly to southwesterly flow advecting high-θ_e air into the Oklahoma–Kansas network region. A sounding at Dodge City, Kansas (see DDC in Fig. 5) already exhibits a nearly saturated air mass below 700 mb with considerable convective available potential energy (CAPE). In fact, satellite imagery shows a well-developed MCS (hereafter termed the *first system*) occurring to the east of DDC over northeastern Oklahoma and southeastern Kansas near this time (see Fig. 6). Severe storms did not take place at DDC, until 2330 UTC 10 June (see JH88) when vertical motion, boundary layer (heating) and other environmental conditions became favorable.

Another feature associated with the present severe squall outbreak is the presence of an upper-level jet streak to the north of the network (see Fig. 3). In particular, the squall line is found to be located in the entrance region of the jet streak during its whole lifetime. The existence of the upper-level jet streak appears to provide a favorable environment for the development of deep convection, since, based upon the mass-momentum adjustment argument by Uccellini and Johnson (1979), there would be a thermally direct circulation transverse in the entrance region of the jet streak with favorable vertical motion over the area into which the squall system was propagating.

4. Numerical simulation

As mentioned earlier, the prediction of the initiation of the 10 June squall line at nearly the right time and

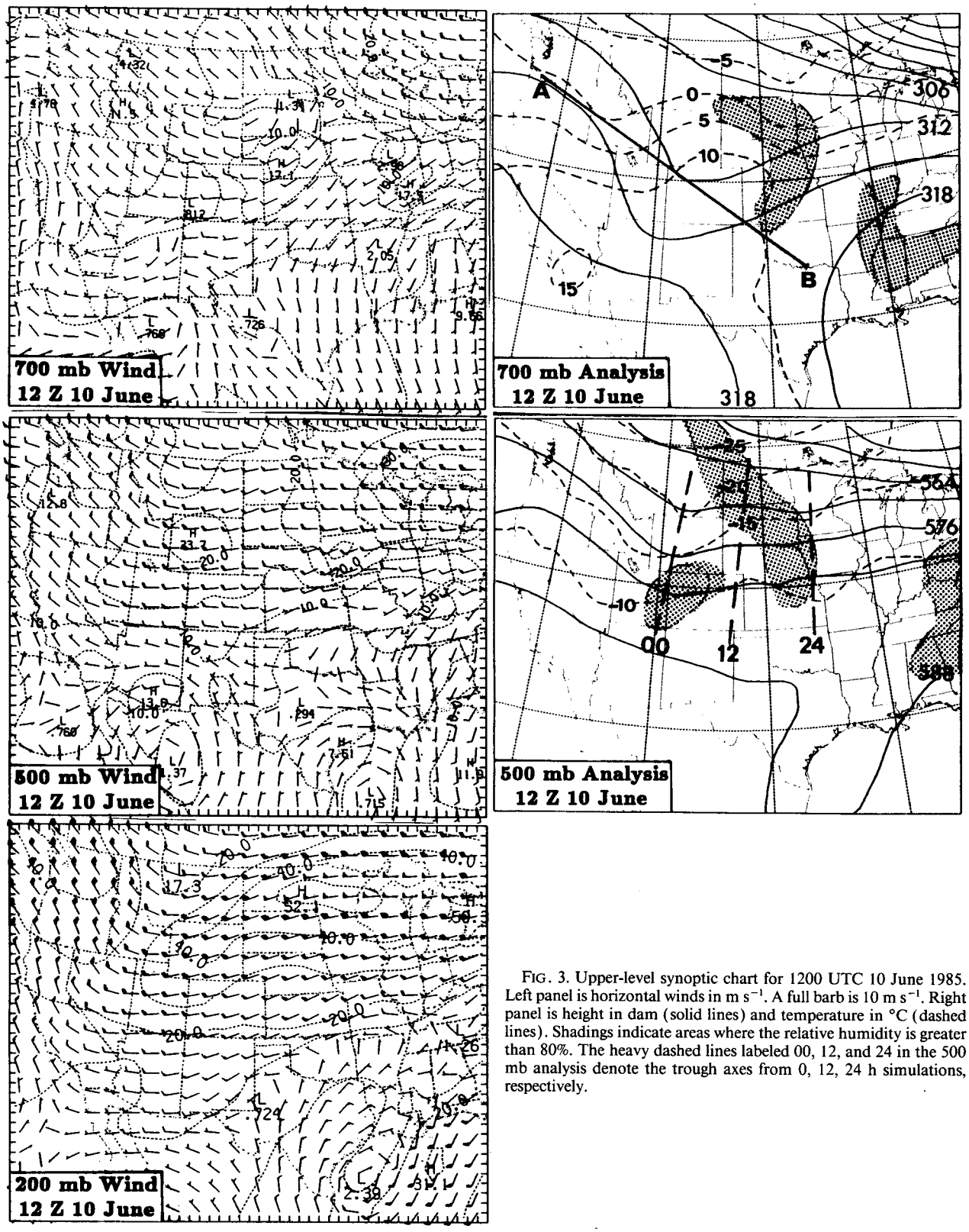

FIG. 3. Upper-level synoptic chart for 1200 UTC 10 June 1985. Left panel is horizontal winds in m s^{-1}. A full barb is 10 m s^{-1}. Right panel is height in dam (solid lines) and temperature in °C (dashed lines). Shadings indicate areas where the relative humidity is greater than 80%. The heavy dashed lines labeled 00, 12, and 24 in the 500 mb analysis denote the trough axes from 0, 12, 24 h simulations, respectively.

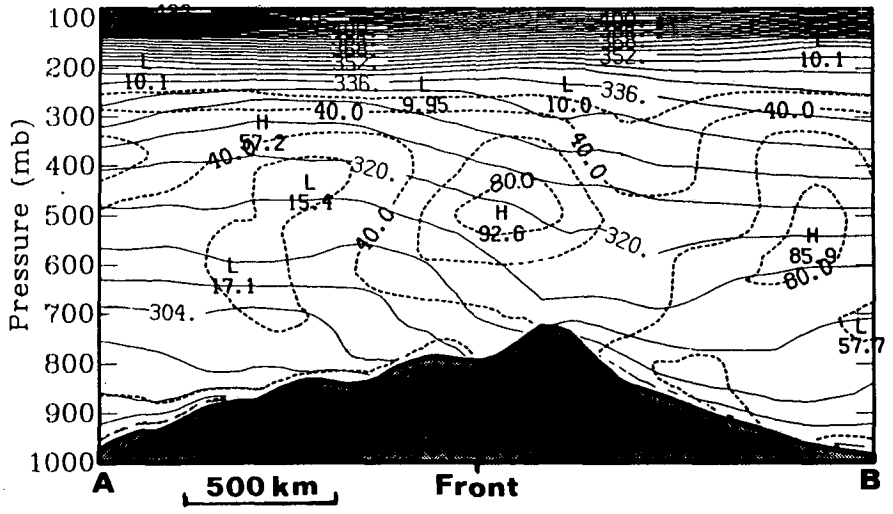

FIG. 4. Cross section along line *AB* in Fig. 3. Solid lines denote potential temperature at intervals of 4 K and dashed lines represent relative humidity (%) at intervals of 20%. The scalloped area is terrain.

location several hours after the model initial time is an important measure of the model's performance. Thus, section 4a describes the simulation of conditions prior to the squall-line development and discusses the mechanisms whereby the squall line was possibly initiated. The investigation of the formation of the 10–11 June squall system is particularly relevant, since this event was not discussed in detail in the previously mentioned observational studies due to the fact that the line formed outside of the PRE-STORM network. Section 4b verifies the simulated surface meso-β scale features against observations. Section 4c discusses the model's performance in reproducing the vertical and midtropospheric structure associated with the squall systems during the mature stage. Section 4d shows the evolution of a mesovortex and its impact on the convective events. Section 4e compares the simulated precipitation structure with the observed. Because of the available high-resolution observations and the evolution of most convective events occurring over the PRE-STORM network region, a large portion of the following comparative studies will be presented in the subdomain framework (see Fig. 1).

a. Simulation of conditions prior to the squall-line development

Although the model was initialized with conventional data, the implicit Fritsch–Chappell convective scheme did not have any difficulty in generating model convection during the first hour of the simulation at a reasonable location as compared to observations (see Fig. 6), since the frontal system, particularly the strong cool pool behind the surface front and associated lifting along its leading edge, provided favorable forcing for the initiation of model convection along the front. Theoretical studies by Hoskins et al. (1984) and Cho and Chan (1987) also show that the presence of mesoscale thermal inhomogeneities is conducive to the mesoscale organization of upward motion and precipitation. Likewise, the model reproduced well the observed widespread convection associated with the first system over the Oklahoma–Kansas area during the first two model hours (not shown). However, due to the coarse resolution and smooth initial conditions and the fact that no balancing between mass and wind fields was performed in preprocessing the initial data, it took more than three hours of model time for adjusting mass and wind fields to a reasonable "noise" level (measured by parameters $\int |\partial p^*/\partial t| \, dxdy$ and $\int |\partial^2 p^*/\partial t^2| \, dxdy$), and for generating certain subsynoptic-scale features comparable to the nature. Thus, Fig. 7 shows the simulated distribution of sea-level pressure, surface (i.e., first model σ level $\sim$ 15 m) temperature, surface streamlines and 6 h accumulated rainfall verified at 1800 UTC 10 June. Continued deep convection over Oklahoma–Kansas region produced widespread and significant rainfall. Associated with it is a mesohigh pressure center with divergent low-level outflow. Although the surface layer in the model over clear air has been heated up for more than 8°C during this 6 h period, surface temperatures under the cloud shield are still similar to those at the initial time. This appears to be due to the effects of cloud shading, and slight cooling produced by moist downdrafts in the near-saturated subcloud conditions (see DDC sounding in Fig. 5). Specifically, a sounding over central Oklahoma (not shown) exhibits near-saturated and moist-adiabatic conditions as compared to the DDC sounding in low- to midtroposphere. These conditions are unfavorable

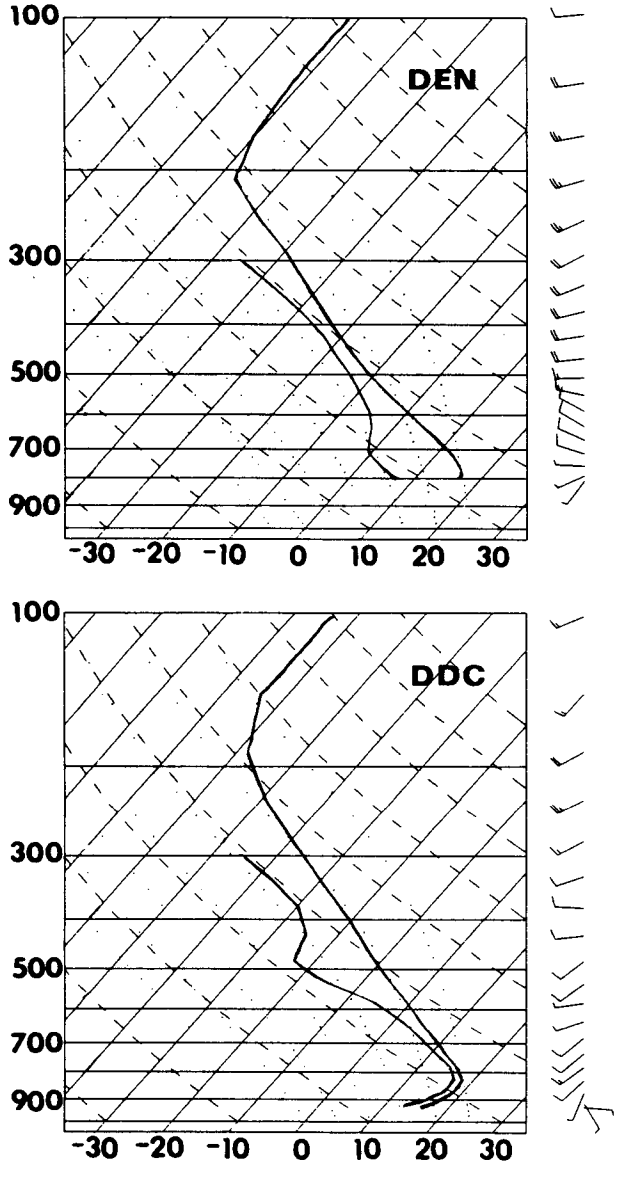

FIG. 5. Upper-air soundings for Denver (DEN), Colorado, and Dodge City (DDC), Kansas, at 1200 UTC 10 June 1985 (see Fig. 1a for the location). A full barb is 10 m s^{-1}.

for the generation of cold downdrafts. Moreover, (parameterized) downdraft parcels can overshoot into much cooler low-level air (e.g., the layer beneath the inversion in the DDC sounding), resulting in warming rather than cooling of the boundary layer.

By contrast, continued convection associated with the advancing cold front during this 6-h period produced much less rainfall (local maximum $\leq$ 4 mm) than that for the first system. Examination of model output indicates that this resulted from a low precipitation efficiency (determined by a parameterized relationship among the precipitation efficiency, vertical wind shear and height of the cloud base in the Fritsch–Chappell scheme; see Fritsch and Chappell 1980; Zhang and Fritsch 1986). Specifically, the relationship states that the stronger the wind shear is, or the higher the cloud base is, the less efficient are the convective clouds and more condensates would be lost to evaporation in moist downdrafts. In fact, as compared to the first system (80%–90%), a much lower precipitation efficiency ($\leq$40%) is expected in view of the wind shear below 500 mb and cloud base inferred from the initial DEN and DDC soundings (Fig. 5). As a result of this low efficiency, the model produces very strong downdraft cooling ahead of the cold front. Even taking into account the terrain effect on the surface temperature distribution, the temperature gradient across the outflow boundary ahead of the frontal zone is quite substantial ($\sim$18°C over 250 km), especially in comparision with that of the first system. Consequently, the thermal structure associated with the cold front has been significantly obscured by the cold outflow. However, the two air streams behind the front now become more clearly apparent. Meanwhile, because of the southward propagation of the cool pool associated with the sector *A* front, the frontal low between the cold and warm fronts was forced to move southeastward in advance of the frontal system. Moreover, a well-defined convergence line developed along the warm front (Fig. 7). Later, the squall line forms as the sector *A* front approaches this convergence line.

A small model convective system and associated mesohigh are triggered ahead of the (sector *B*) frontal system around 1500 UTC (Fig. 7). This system formed in association with the strong cold outflow from the frontal convection, and appears to correspond to an observed area of convection ahead of the southwestern end of the frontal cloud system (cf. Figs. 6b and 7) which eventually became the trailing southwest extension of the squall line. However, in the model, it is clearly too strong and extensive, and propagates too fast. This discrepancy is most likely caused by the imperfect and too coarse initial conditions (see Fig. 1b for the sounding distribution). Specifically, the thermodynamic information at Grand Junction (i.e., the station over western Colorado) may have influenced on too extensive an area to the east by the objective analysis-initialization scheme.

At 2100 UTC 10 June (i.e., 9 h into simulation), the overpredicted convective system has moved much farther ahead of the sector *B* front (Fig. 8). Around this time, a line of convection associated with the sector *A* front developed in the model and began to produce precipitation. The timing of the initiation of this convective line is quite close to the observed squall line, but its location is slightly too far ($\sim$50–60 km) to the north (cf. Figs. 6 and 8). However, this offset is deemed to be adequate for employing the simulation to investigate how the squall line was triggered. Figure 9 shows the simulated sea-level pressure distribution between 1600 and 2100 UTC. During the first three hours of

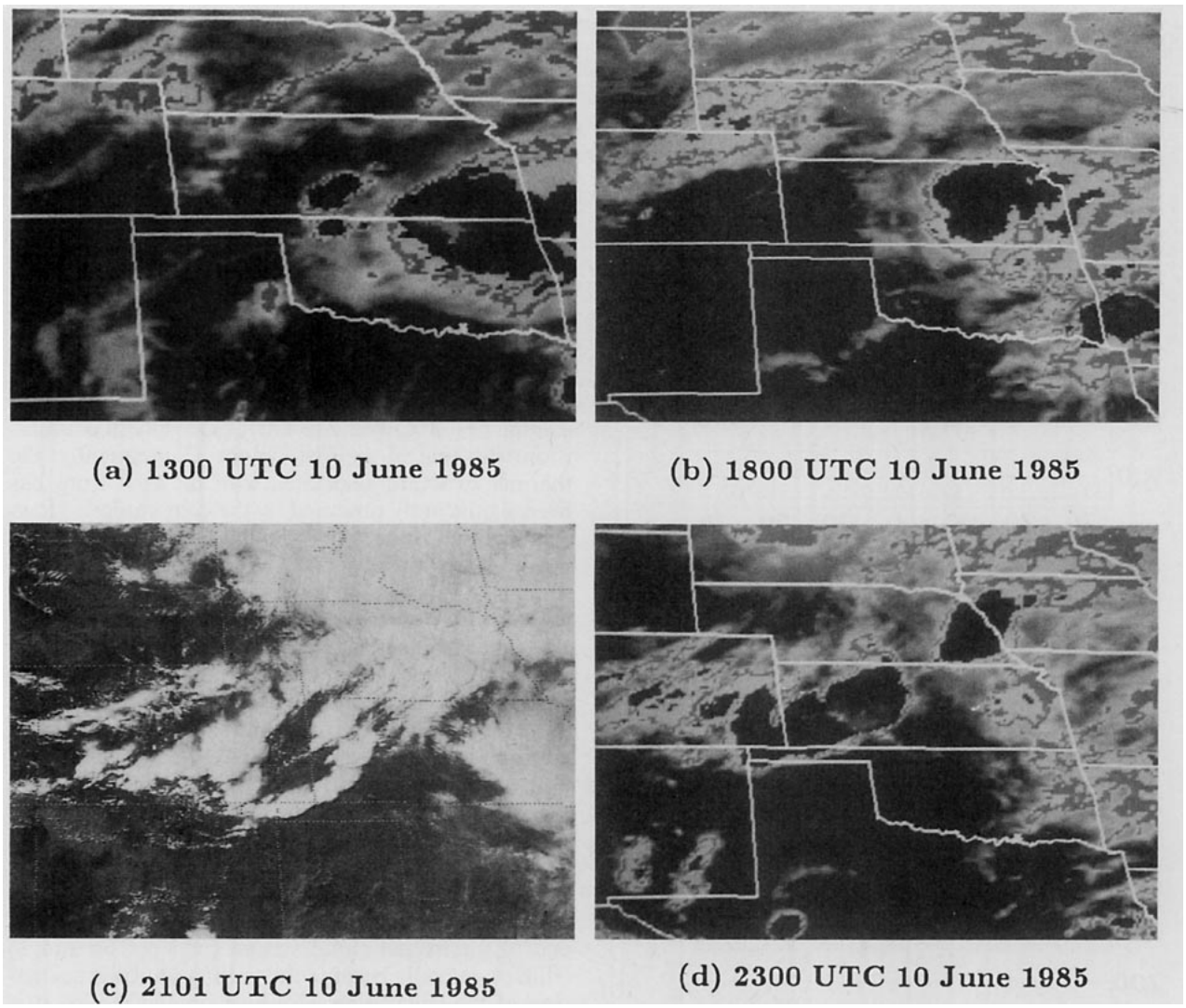

FIG. 6. GOES-1 visible and infrared satellite imagery for the times indicated.

the model adjustment, the movement of the cold front was very slow, probably due to the upwind-side retardation produced by the Rocky Mountains (see Zehnder and Bannon1988). In fact, after the simulated front passed over the continental divide around 1900 UTC, the convective system underwent significant acceleration. Although the position of the overpredicted convective system ahead of sector *B* front looks like the observed squall line, this overpredicted system gradually decayed after 1600 UTC as if it took place in unfavorable larger-scale conditions. The observed squall line did not appear in the model until the sector *A* cold front converged with southeasterly low-level high-θ_e air over western Kansas around 2000 UTC.

An interesting feature in the present case is the generation of several convective bands visible in satellite imagery at 2100 UTC (see Fig. 6). As shown by the 600 mb vertical motion (ω, μb s^{-1}) and relative humidity in Fig. 10, the model produced reasonably well three major convective bands with upward motion and higher contents of moisture. (Note that the southern tail of the first band was generated by the overpredicted system ahead of sector *B* front, and thus is not real.) Hourly rainfall rate also indicate the banded structure (Fig. 8). Note that when the Anthes–Kuo type of convective scheme was utilized for the fine mesh, the model failed to produce these convective bands (not shown), and, needless to say, the squall line. It appears that without the downdraft enhancement, the cold front weakened with time due to continued downslope adiabatic warming and daytime boundary-layer heating. In fact, the Limited-area Fine-mesh Model initialized at 1200 UTC, the same time as in the present case, was also unable to predict any precipitation associated with the squall line. Thus, it appears likely that any numerical models lacking physical mechanisms to pro-

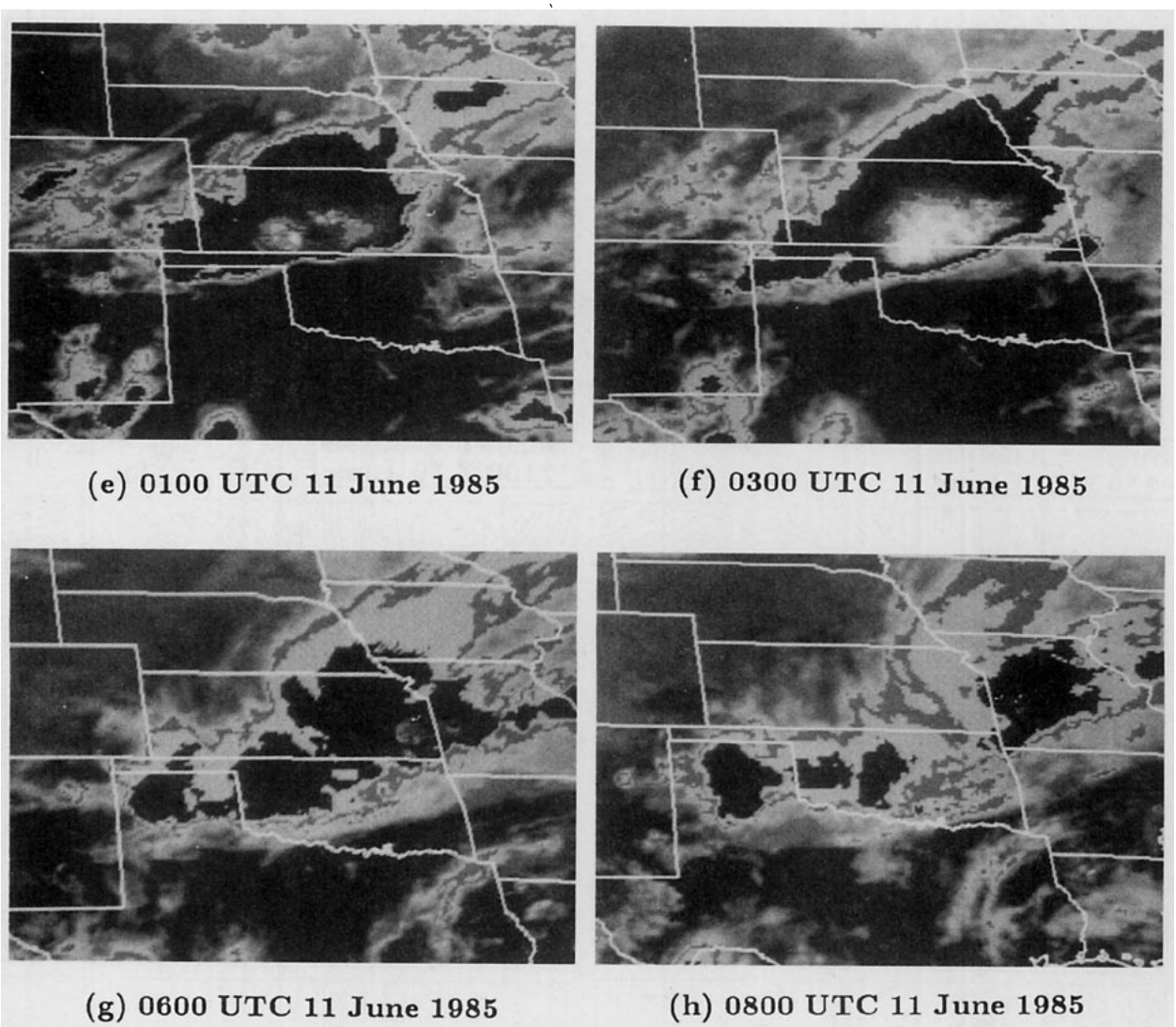

FIG. 6. (*Continued*)

duce cold downdrafts would fail to generate those banded structures, and the realistic development of the squall line. The development of the first system tends to slightly slow down the eastward movement of the squall line after 2100 UTC but does not have any significant effect on its initiation. This conclusion was obtained from an experiment in which the first system was artificially not allowed to develop during the first nine model hours (not shown).

Before turning to the next subsection for detailed model verification, we compare a simulated prestorm sounding with an observed one (Fig. 11) at a place where the severe weather events occurred (i.e., near DDC, Kansas). Both soundings were taken about 2½ hours before the arrival of the squall line. The model simulates reasonably well the DDC sounding except that the lowest 80 mb of the mixed layer was 2°C too cold. This is probably due to the simulated first system being too extensive in the west (see Fig. 6). Note the strong capping inversion between 800 and 850 mb that is generally considered a "lid" acting to prevent release of convective instability (Carlson and Ludlam 1968). Based upon the traditional conceptual model, one might expect decaying instead of intensifying of the squall line as it propagated eastward. The simulation reveals that as the favorable upward motion associated with the squall line, particularly the downdraft outflow, approached and as the surface heating carried on, the inversion rapidly weakened and the lower troposphere became more moist and conditionally unstable. This process took place within just *one to two hours.*

b. Simulation of surface features during the mature stage

Between 2100 and 0000 UTC, both the observed and simulated squall lines became well developed and gradually entered the network. Thus, the high-resolu-

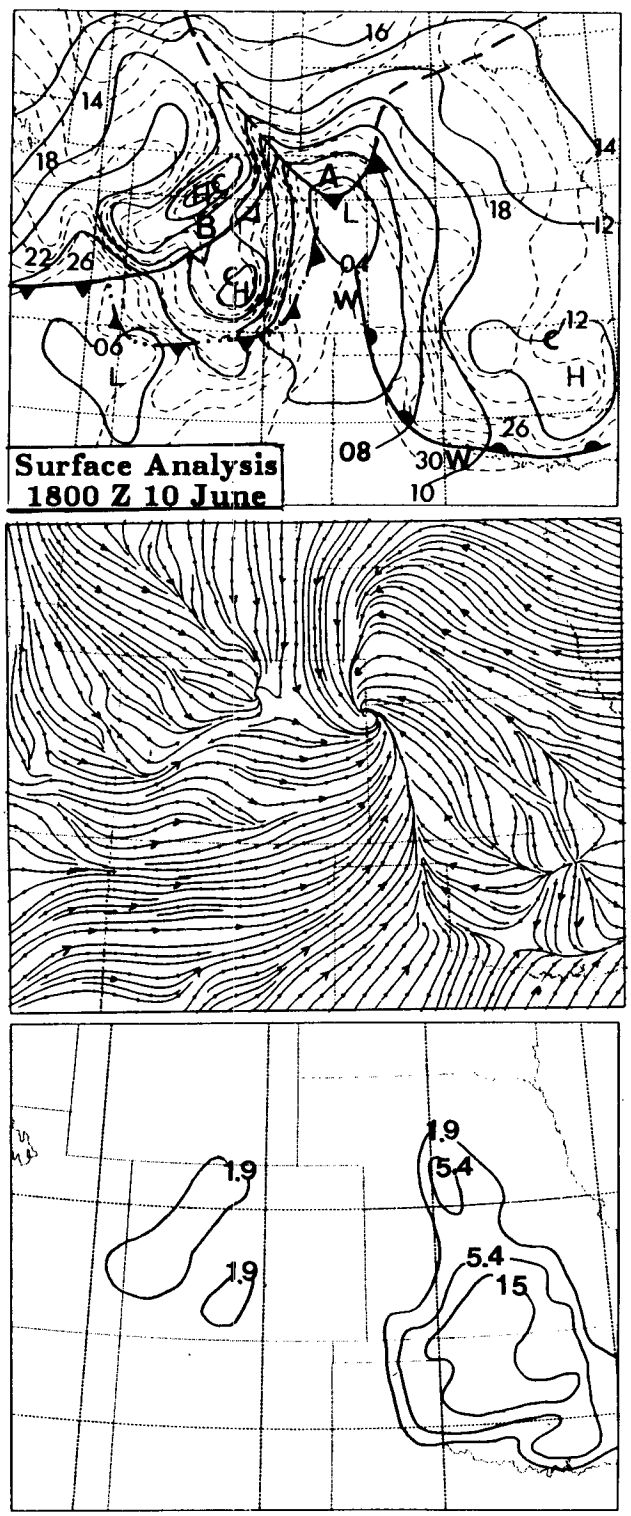

FIG. 7. As in Fig. 2 but for 6-h forecast verified at 1800 UTC 10 June. Cold frontal symbols alternated with double dots indicate moist-downdraft outflow boundaries and open triangles denote obscured location of the front. (c) The predicted 6-h accumulated rainfall (mm) for the period 1200–1800 UTC 10 June.

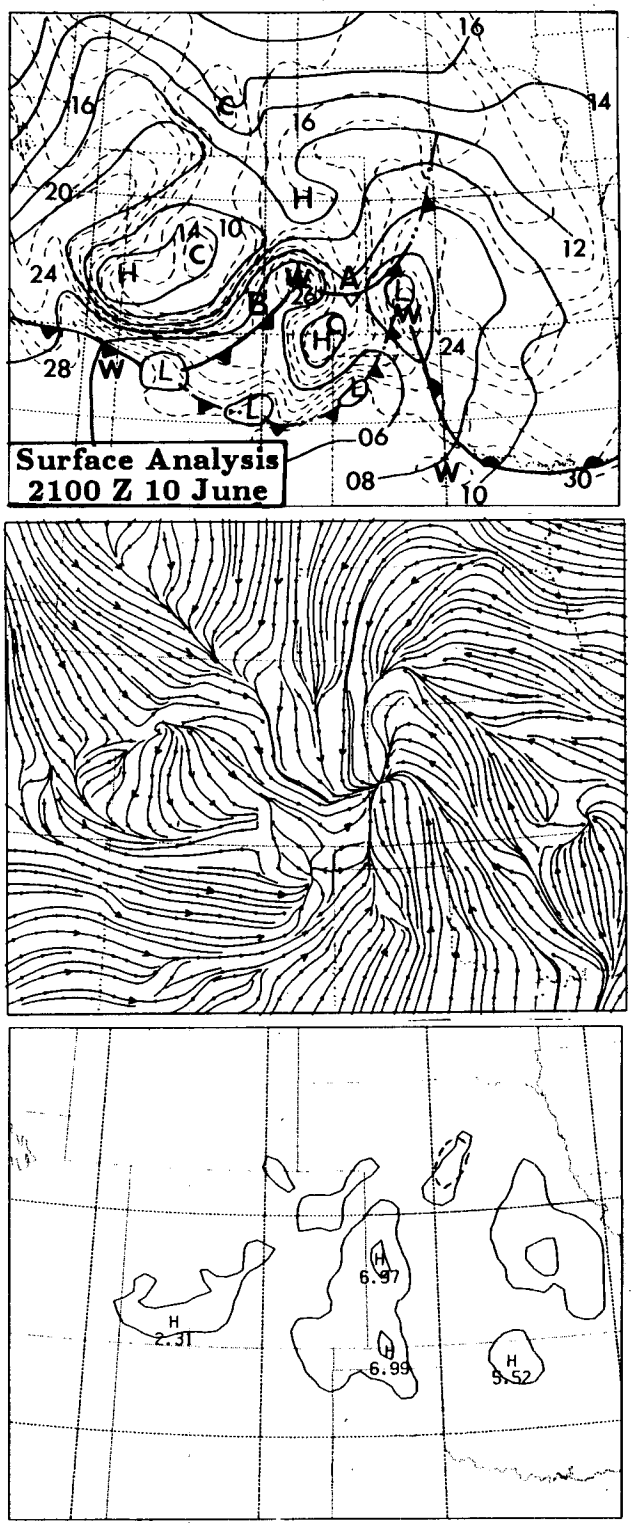

FIG. 8. As in Fig. 2 but for 9-h forecast verified at 2100 UTC 10 June. (c) The predicted hourly rainfall rate at intervals of 5 mm h^{-1} beginning with 1 mm h^{-1} isohyet at 2100 UTC 10 June. Solid lines are for the implicit rainfall rate and dashed lines are for the explicit rainfall rate.

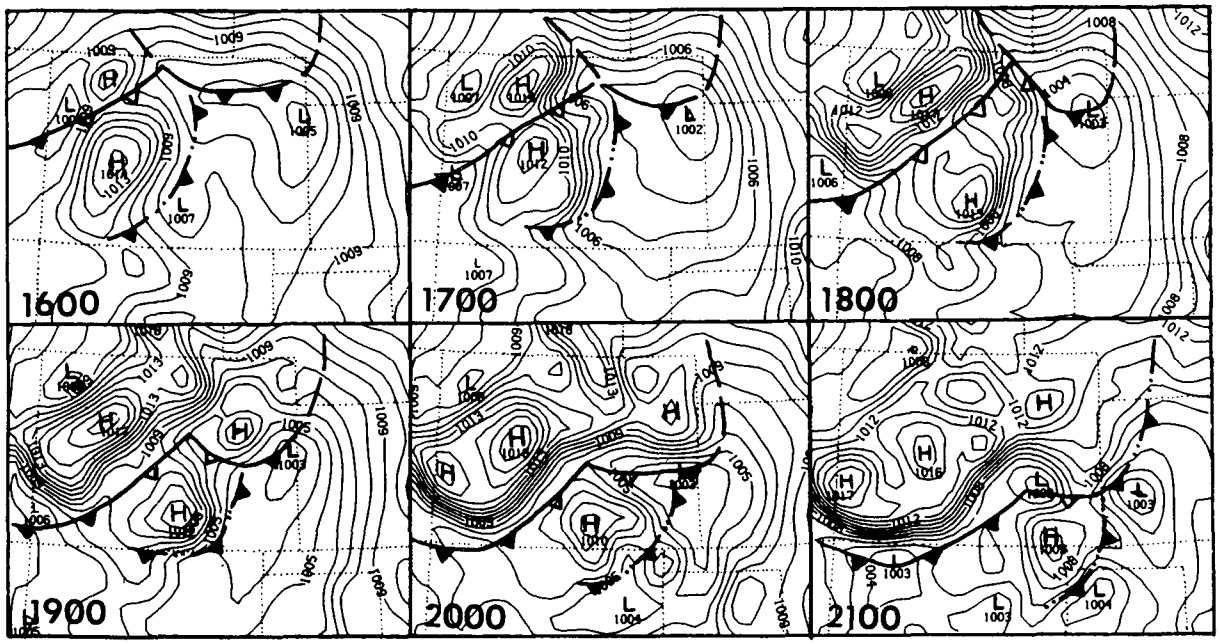

FIG. 9. Distribution of the simulated sea-level pressure (mb) from 1600 to 2100 UTC 10 June.

tion network data became available for model verification. Figures 12a–f compare the simulated surface variables, such as sea-level pressure, temperature, moisture, stream line, convective and stratiform rainfall distribution to the observations from JH88, R88 and our objective analysis. The model squall line is well represented by the hourly rainfall rate distribution, although at this time the rainfall associated with the decaying first system somewhat obscures the line structure. Note that the JH88 observational pressure analysis was performed by converting surface pressure reports to a PAM (Portable Automated Mesonetwork) station-averaged elevation of 518 m; thus absolute comparisons of the reference pressure values between forecasts and observations are not possible. In spite of this difference in converting surface pressures, comparisons of the simulated surface features with the JH88 analysis, and hourly rainfall rate at 0000 UTC with the R88 radar echo pattern at 0103 UTC reveal that the model squall line still lags 1 h of translation distance (~50 km or 2 grid increments) behind the observed events. Figure 13 shows comparisons of hourly position of the squall line between forecasts and the Vasiloff and Bluestein (1988) analysis. Both observed and simulated systems

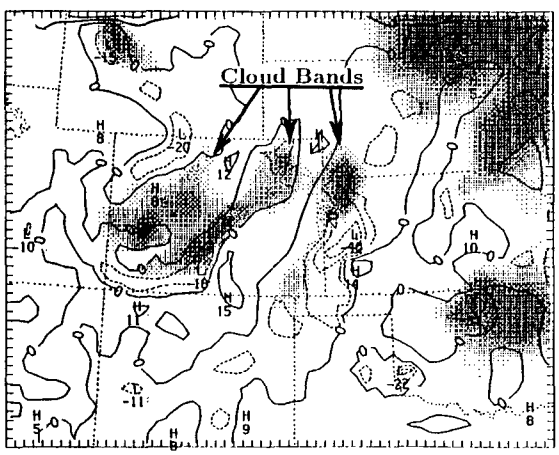

FIG. 10. Distribution of the 600 mb relative humidity (more than 80% is shaded) and vertical motion (ω, $\mu b\ s^{-1}$) from 9-h simulation, verified at 2100 UTC 10 June. Dashed lines indicate upward motion and solid lines indicates downward motion.

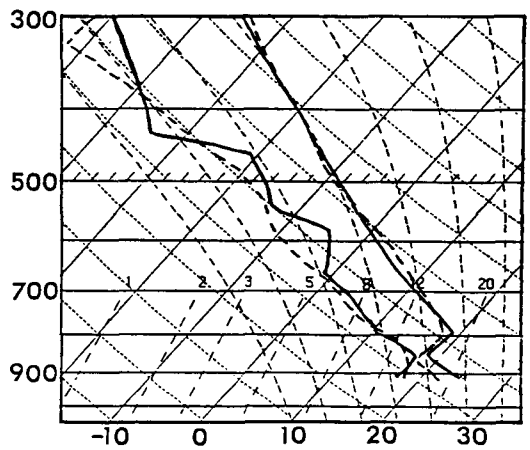

FIG. 11. Comparison of the observed (solid) upper-air DDC, Kansas, sounding to the simulated (dashed) for 2100 UTC 10 June.

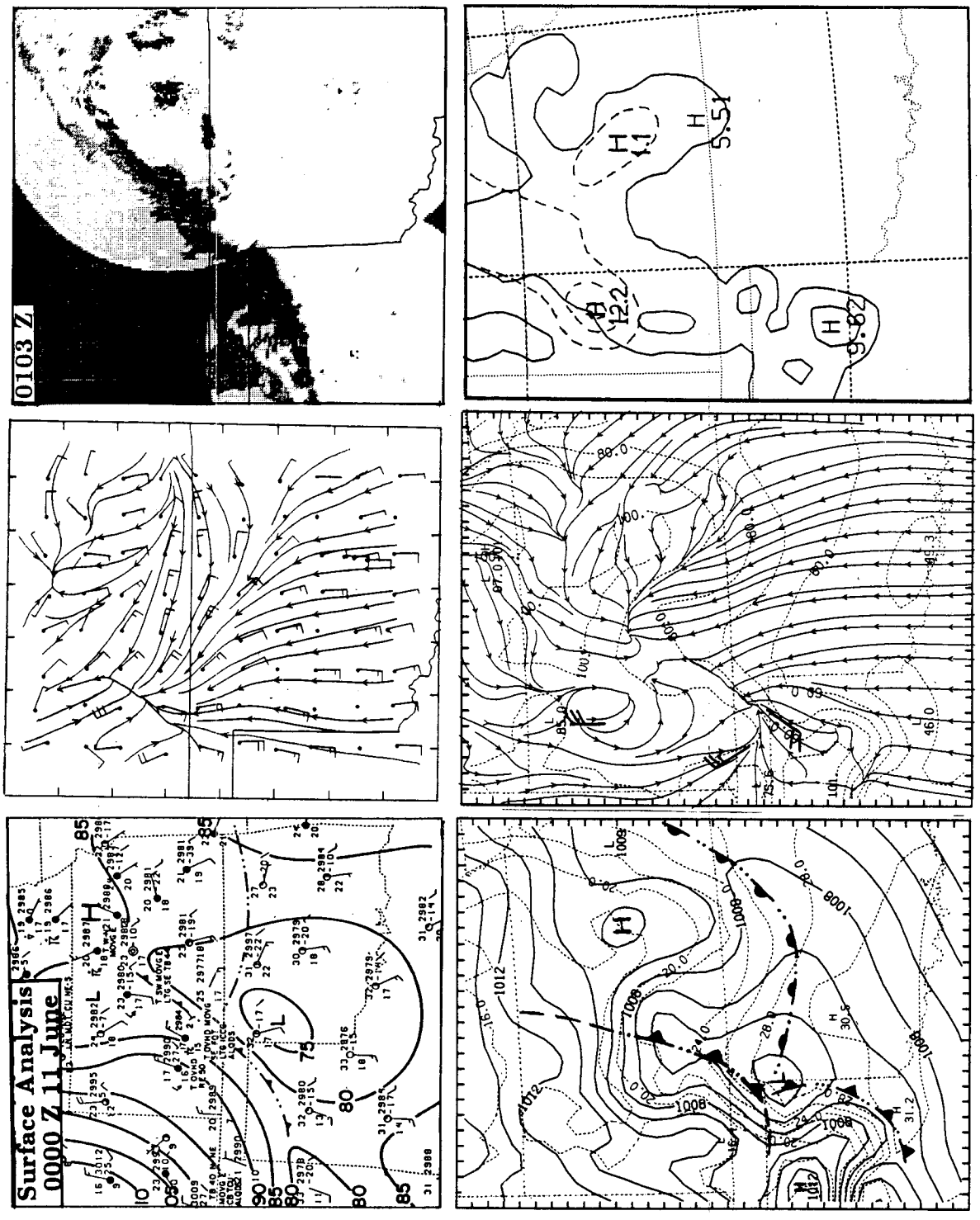

FIG. 12. Upper panel from left to right shows the JH88 surface analysis (pressures are converted to 518 m. Units are in Hg, e.g., 85 = 29.85 in Hg.) for 0000 UTC 11 June, objectively analyzed surface flow (a full barb is 5 m s^{-1}), and the R88 radar analysis for the indicated time, respectively. Lower panel from left to right shows the simulated 12-h distribution of sea-level pressure (solid) and temperature (dashed), surface streamline and relative humidity (dashed), and hourly rainfall rate (at intervals of 5 mm h^{-1} beginning with 1 mm h^{-1} contour), respectively. Convective and the resolvable-scale rainfall rates are denoted by solid and dashed lines, respectively. The simulated local strong surface winds are plotted with a full barb of 5 m s^{-1}.

propagated southeastward with a speed of 14–16 m s^{-1}. The isochrones of the squall line also indicate the 50 to 60 km offset. Despite this offset, we consider the forecast to be accurate enough to demonstrate the model's ability in simulating the evolution of the squall line. Note that the isochrones in Fig. 13 differ a little from the JH88 analysis, since we determined the locations according to convective rainfall whereas in JH88 they are specified according to the position of gust fronts.

It is evident that the model exhibited skill in reproducing the distribution of a presquall mesolow and a weak squall-induced mesohigh. The term 'presquall mesolow' is used hereafter instead of the frontal low since convective forcing gradually overwhelmed the frontal forcing in controlling the structure of the surface pressure field. JH88's pressure-departure analysis data at 2300 UTC also shows a mesohigh associated with the squall line (see Fig. 13a in JH88). Likewise, a retreating outflow boundary associated with the remnant of the first system over northern Oklahoma was reasonably simulated. Evaporation of resolvable-scale condensates left a mesohigh to the north of the outflow boundary. This suggests that the boundary-layer and convective parameterization schemes, and the explicit moisture physics in the model are realistic enough to reproduce the evolution of the squall events. In particular, the simulated surface temperature and moisture under both clear air and cloud shields as well as their gradients at the end of this daytime heating cycle compare favorably to the surface reports. For example, the model produced about 12°–14°C temperature gradient across the squall-generated cold outflow boundary in comparison to the observed gradient of 13°–15°C.

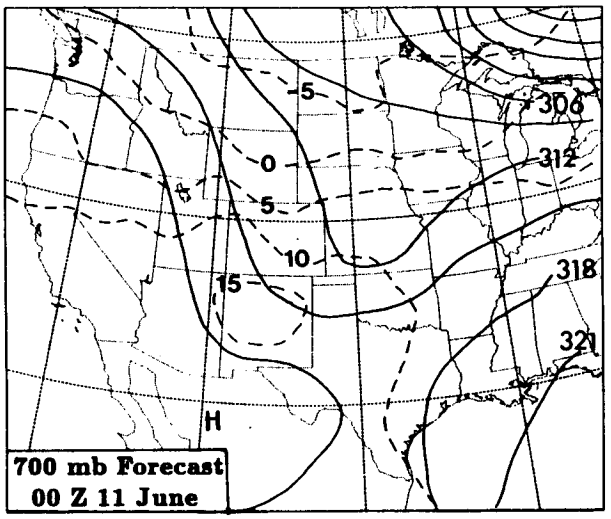

FIG. 14. Distribution of the 700 mb geopotential height (solid lines, dam) and temperature (dashed lines, °C) from 12-h simulation, verified at 0000 UTC 11 June.

Strong cooling of 17°C was reported behind the squall line over southwestern Kansas whereas a corresponding 16.4°C surface temperature deficit was simulated. Both observations and the simulation show a relatively warm and dry PBL to the east of the squall system. Meanwhile, the model simulated very strong surface convergence near the intersection of the squall-line outflow and the warm front. This location is coincidentally the place where a tornado, hail and wind gust were reported. The result indicates that high-resolution mesoscale models can become a very useful tool in the

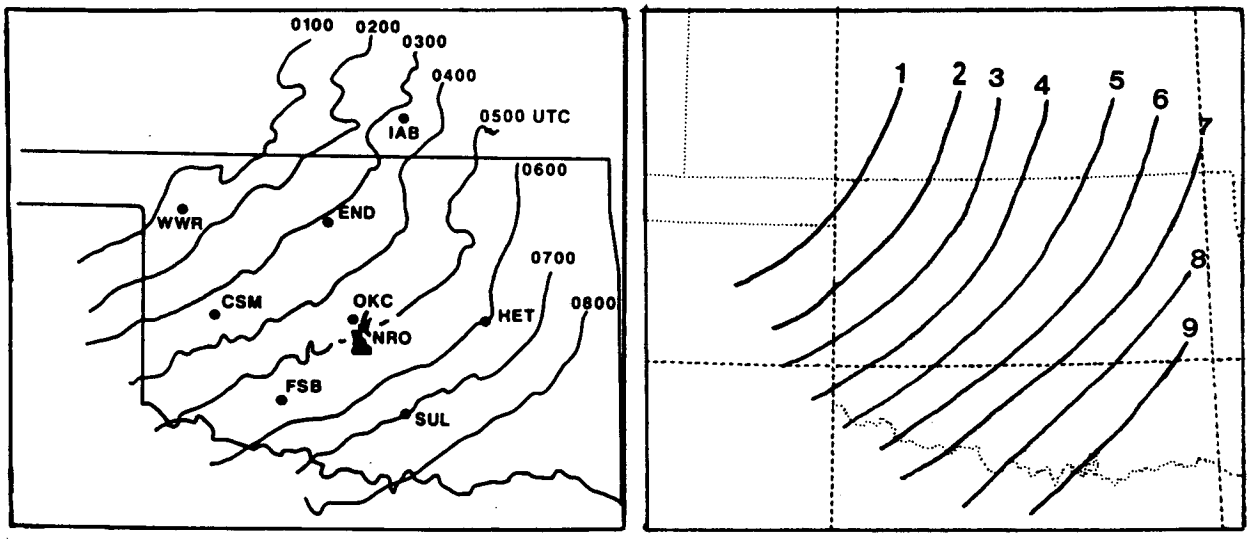

FIG. 13. Comparison of (a) the observed hourly position of the squall line (from Vasiloff and Bluestein 1988) to (b) the simulated over the period 0100 and 0900 UTC 11 June.

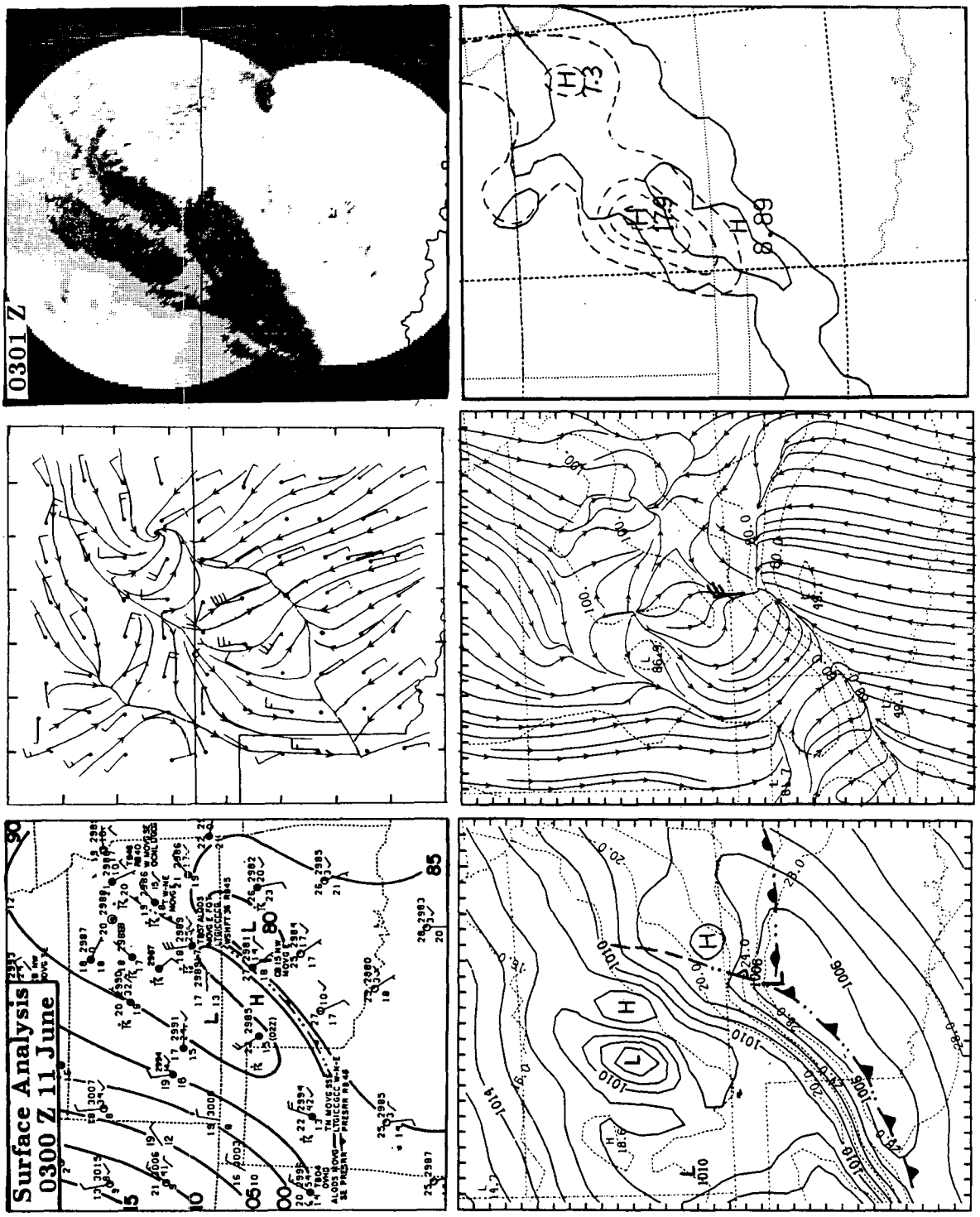

FIG. 15. As in Fig. 12 but for 0300 UTC 11 June.

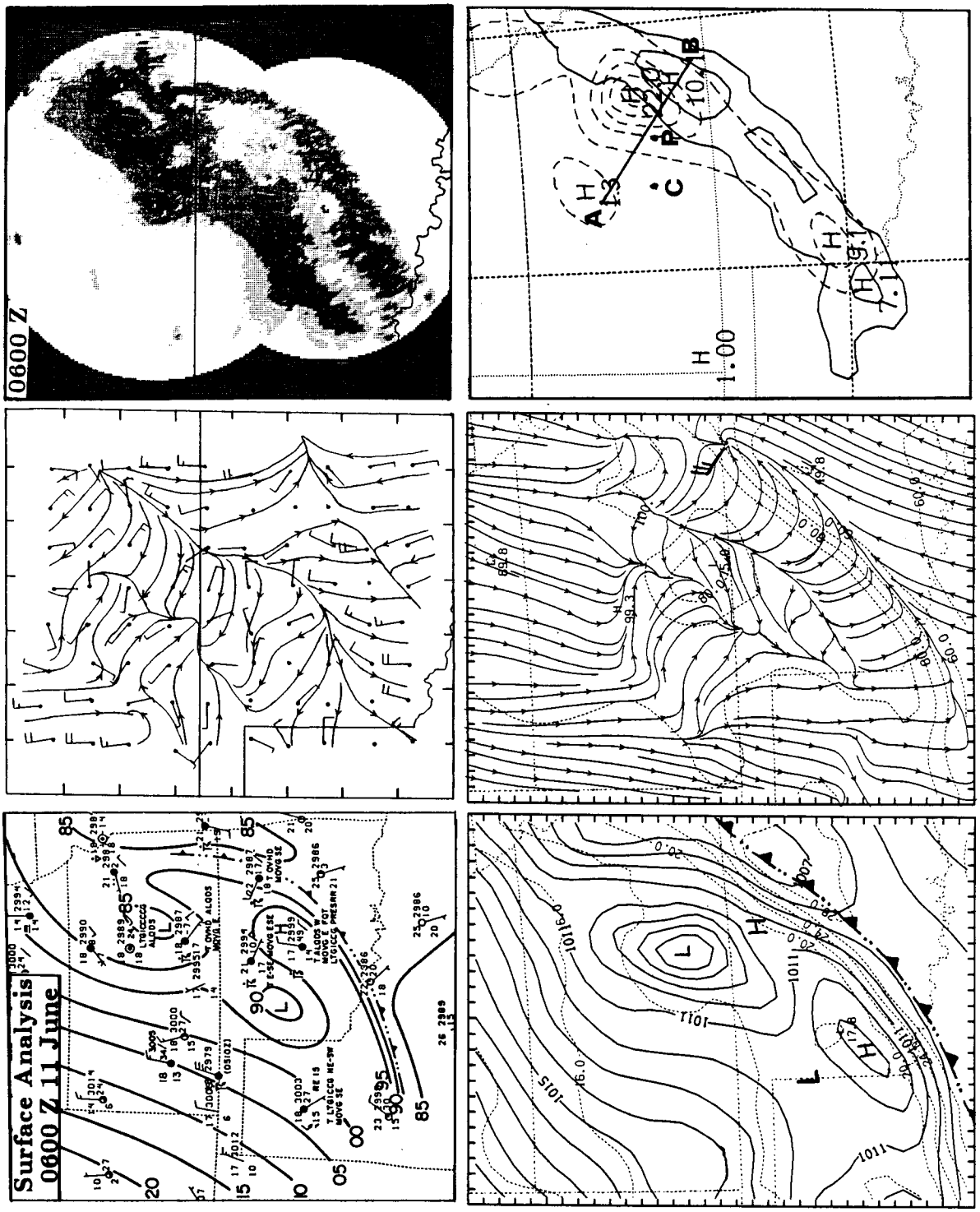

FIG. 16. As in Fig. 12 but for 0600 UTC 11 June.

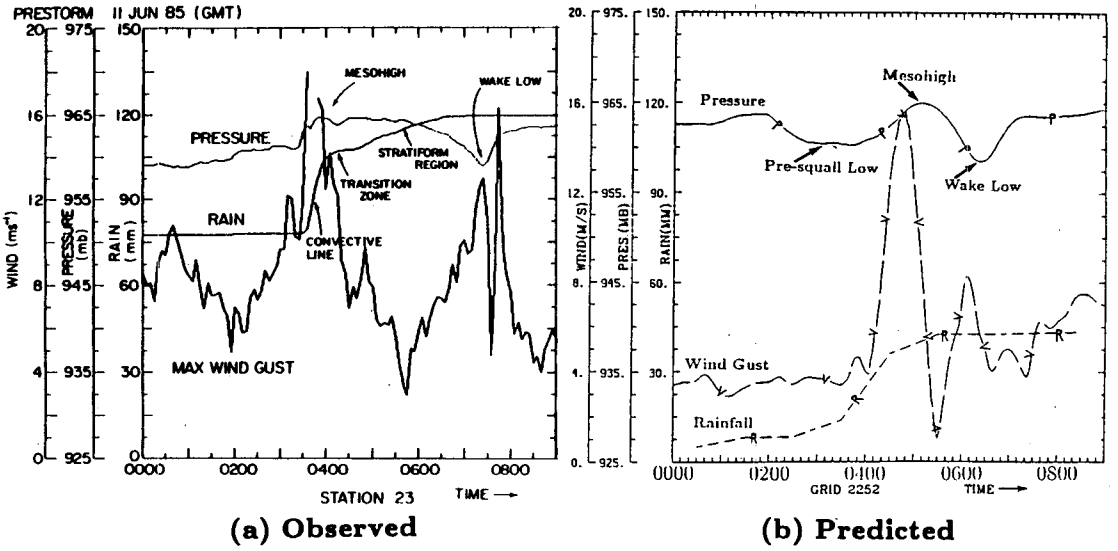

FIG. 17. Comparison of the time series of (a) the observed pressure, rainfall and horizontal wind at PAM station 23 (from JH88) to (b) the simulated (see Fig. 16 for the location '*P*').

future in assisting the issuance of severe weather warning if additional numerical case simulations are successful. The mechanism whereby the severe weather developed in this case appears to be similar to that illustrated by Purdom (1976), namely, through the thermal boundary interaction. Maddox et al. (1980) also showed several examples in which interaction of thunderstorm outflow with a warm front tends to increase the severity of convective activity.

Other well-simulated features include (i) the strong low-level convergence of southerly winds with northerly flows along the outflow boundary; (ii) the development of resolvable-scale precipitation to the rear of the convective rainfall; and (iii) the amplification of the shortwave trough below 500 mb and persistent cold advection behind the trough axis (see Fig. 14 for the 700 mb pattern). From the simulation, the location and southeastward propagation of the convergence line are

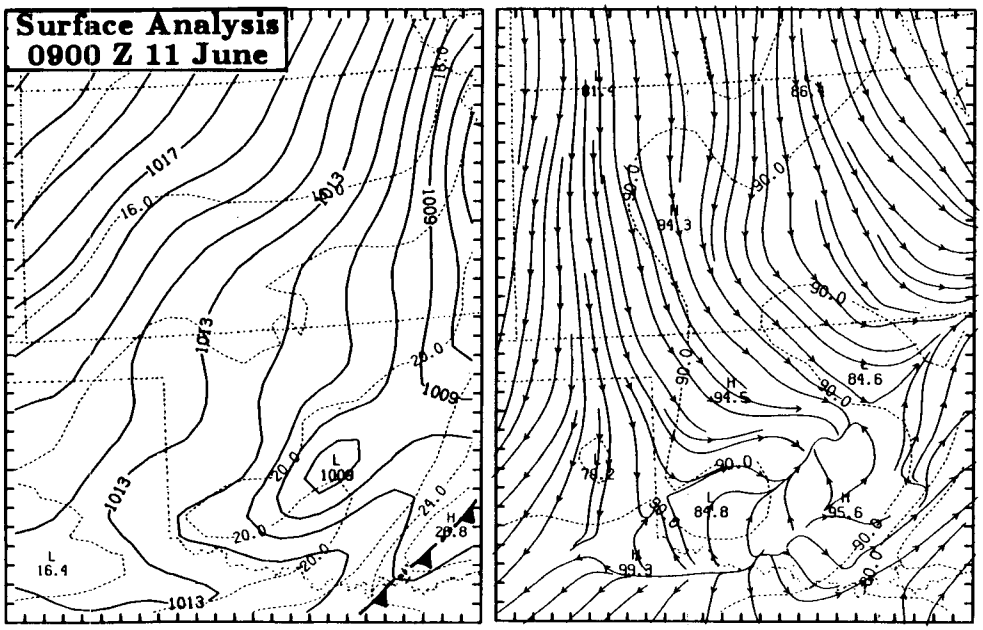

FIG. 18. Distribution of the sea-level pressure (solid lines, mb) and temperature (dashed lines, °C); surface flow and relative humidity from 21-h simulation, verified at 0900 UTC 11 June.

closely related to the northerly intruding cold air behind the sector *A* front with enhancement from convective downdrafts and resolvable-scale evaporation and melting. The propagation and orientation of the mid-tropospheric trough axis correspond to the development of the squall line. Evidently, the short-wave provided another potential forcing mechanism besides the surface front for assisting the initiation and organization of deep convection into the line structure. The vertical latent and sensible heat transport by deep convection may in turn help intensify the short-wave.

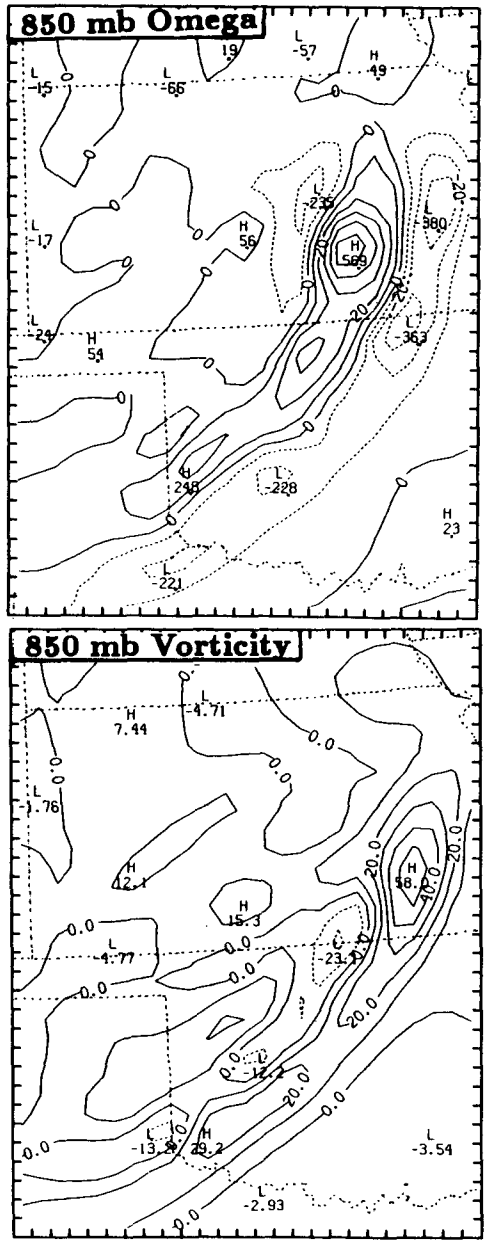

FIG. 19. Distribution of the 850 mb vertical motion (ω) at intervals of 10 μb s^{-1} and relative vorticity at intervals of 10^{-4} s^{-1} from 18-h simulation, verified at 0600 UTC 11 June.

Above 600 mb, the amplitude of the short-wave decreases, and thus only the simulated trough axis is shown in Fig. 3.

After 0000 UTC 11 June, the observed squall line substantially intensified and the stratiform clouds expanded very rapidly. By 0100 UTC, the system satisfied the size (but not the shape) criteria of an MCC (see Fig. 6) as defined by Maddox (1980). According to R88 and JH88, the squall line reached its maximum intensity and coverage over the period 0200–0400 UTC. At 0300 UTC, an important feature, the wake low, became well developed at the back edge of the stratiform region. The formation of a strong wake low is usually considered as a characteristic of mature squall lines (Fujita 1963; Pedgley 1962). While the squall line was intensifying, the boundary layer sustained significant cooling as a result of upward longwave radiation after sunset.

In general, the simulated squall system around 0300 UTC conforms to the observational analyses (Fig. 15). It is particularly noteworthy that the model accurately reproduces the wake low to the rear of the squall line. In the model, this low is found to be first evident around 0100 UTC. As will be shown in a subsequent paper, the wake low results hydrostatically from mesoscale subsidence associated with subsiding flow entering the squall line in a rear-inflow jet. The simulated mesohigh between the presquall and wake lows is well maintained and actually has become strengthened from that of 3 h before. The generation of the model mesohigh is considered to be a consequence of the parameterized moist downdrafts and resolvable-scale evaporation, as has also been shown in Zhang and Fritsch (1986) and Zhang et al. (1988). The strongest pressure gradient across the squall line during its lifetime was simulated, indicating that the model squall line has reached its mature stage as it did in reality. Due to the surface pressure distribution, three well-defined confluence, diffluence and confluence axes developed in both the observations and simulation. Apparently, these flow structures are determined by the strong pressure gradient between the presquall mesolow, mesohigh and wake low. The formation of the wake low considerably changed the low-level flow structure (cf. Figs. 15 and 12).

In addition to the intensification of the surface pressure field, both the observed and simulated convective and stratiform rainfall increased and expanded between 0000 and 0300 UTC. The rainfall rate distribution resembles quite well the cloud and rainfall coverage from both satellite imagery and radar echoes. The continued deepening of the squall system as the boundary layer kept cooling indicates that the larger-scale forcing and downdraft outflow may play a dominant role in initiating new convection along the leading edge.

Although the squall line rapidly decayed after 0400 UTC, many meso-β scale features are best defined around 0600 UTC 11 June. These include the trailing

stratiform clouds, the wake low, surface convergence–divergence flow structure and a rear-inflow jet. Thus, this is a crucial time in the integration for testing the model's performance. Figure 16 compares the 18-h simulated surface distribution valid at 0600 UTC to the corresponding observational analysis. The model

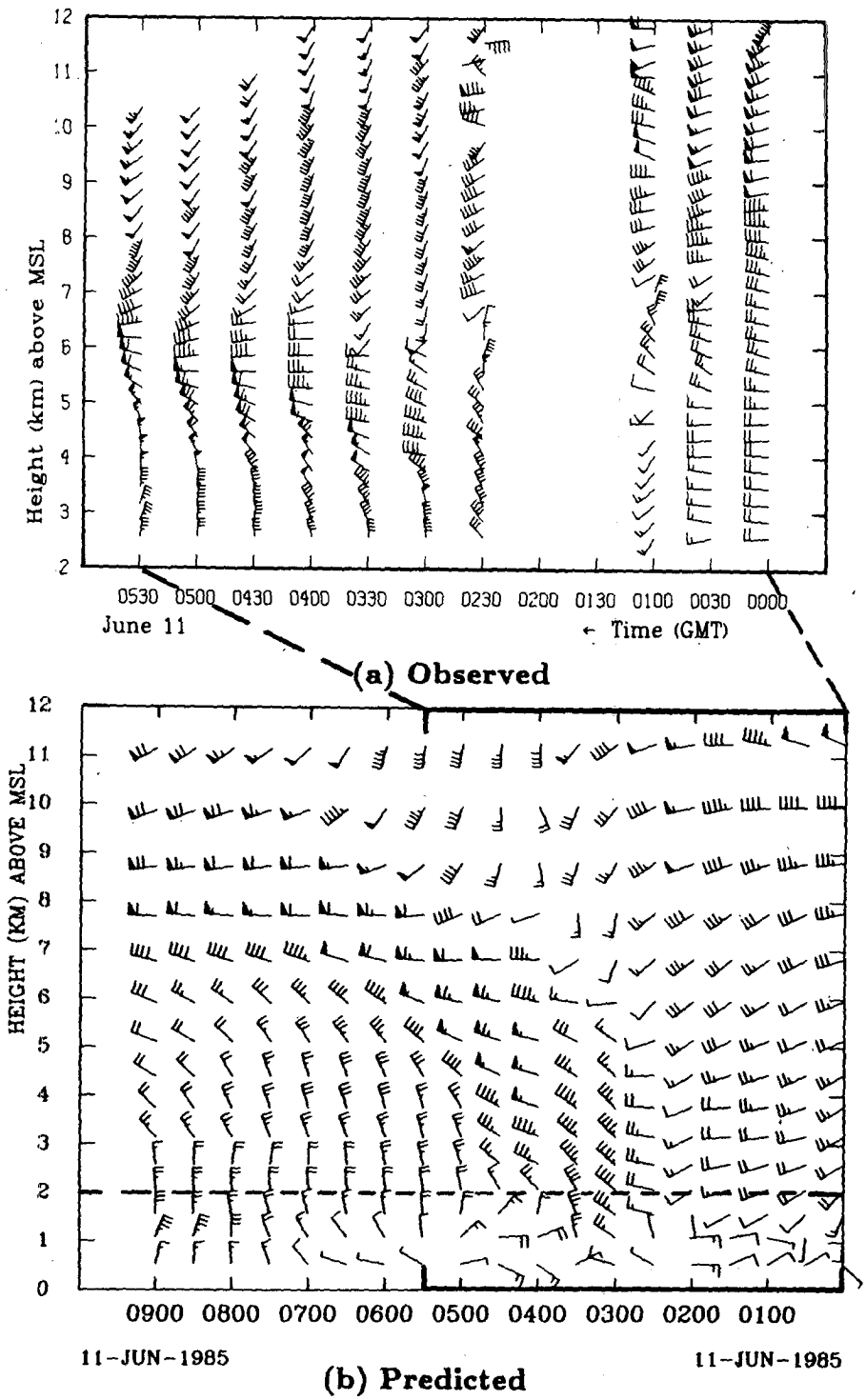

FIG. 20. Comparison of (a) the observed profiler wind (adapted from Augustine and Zipser 1987) to (b) the simulated at McPherson, Kansas (see Fig. 1 for the location *M*). A full barb is 5 m s^{-1}. Dashed lines are drawn for the purpose of emphasizing the different vertical domains associated with the simulations and observations.

simulated quite well all the above-mentioned mesoscale features, including the splitting of the wake low and shrinking of convective rainfall coverage. Only the intensity of the wake low appears to be somehow overpredicted. The maintenance of the wake low for more than 6 h in this case suggests that this feature has a time scale more than 50% of the lifetime of squall lines and thus is not a transient meso-β scale phenomenon. These results are particularly encouraging when considering that all these meso-β scale features are gen-

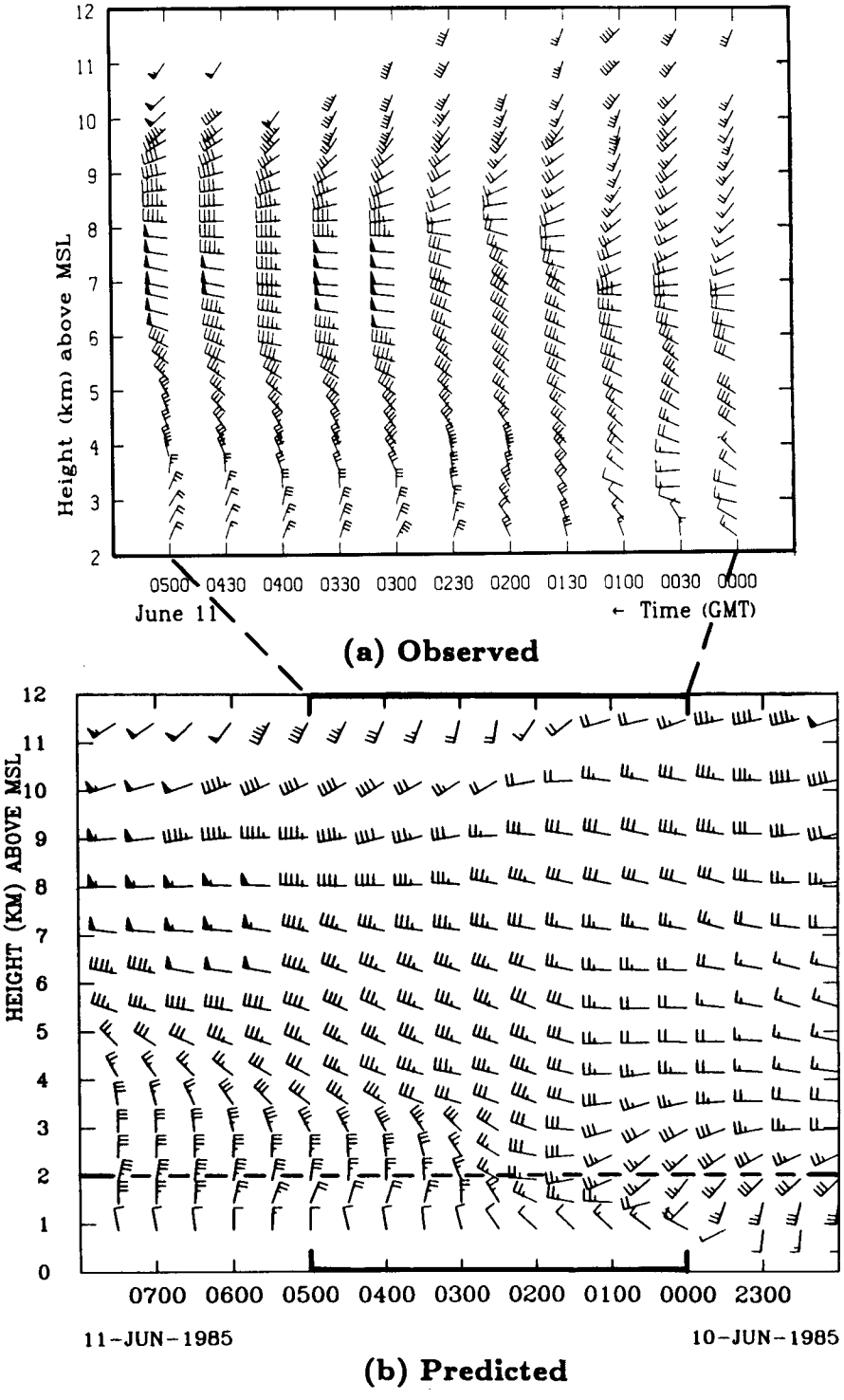

FIG. 21. As in Fig. 20 but for Liberal, Oklahoma (see Fig. 1 for the location L).

erated from conventional-data produced initial conditions.

In order to further demonstrate the model's capability in reproducing the surface features associated with the squall line. Figure 17 compares the simulated surface traces of pressure (mb), wind speed (m s^{-1}) and rainfall (mm) to that observed at PRE-STORM PAM station 23. Although the simulated details differ somewhat from the observed, the general comparison of their trends is favorable. Specifically, after the simulated presquall trough axis passed, convective rainfall began, followed by a wind gust of about 16 m s^{-1}. This gust corresponds to a pressure jump of more than 4 mb within 1–2 h, and can be traced back to the simulated 0000 UTC surface gust near the observed location of the severe storm. As shown in Figs. 12, 15, and 16, the gust winds appear to be isallobaric and are certainly highly ageostrophic (i.e., almost 90° perpendicular to

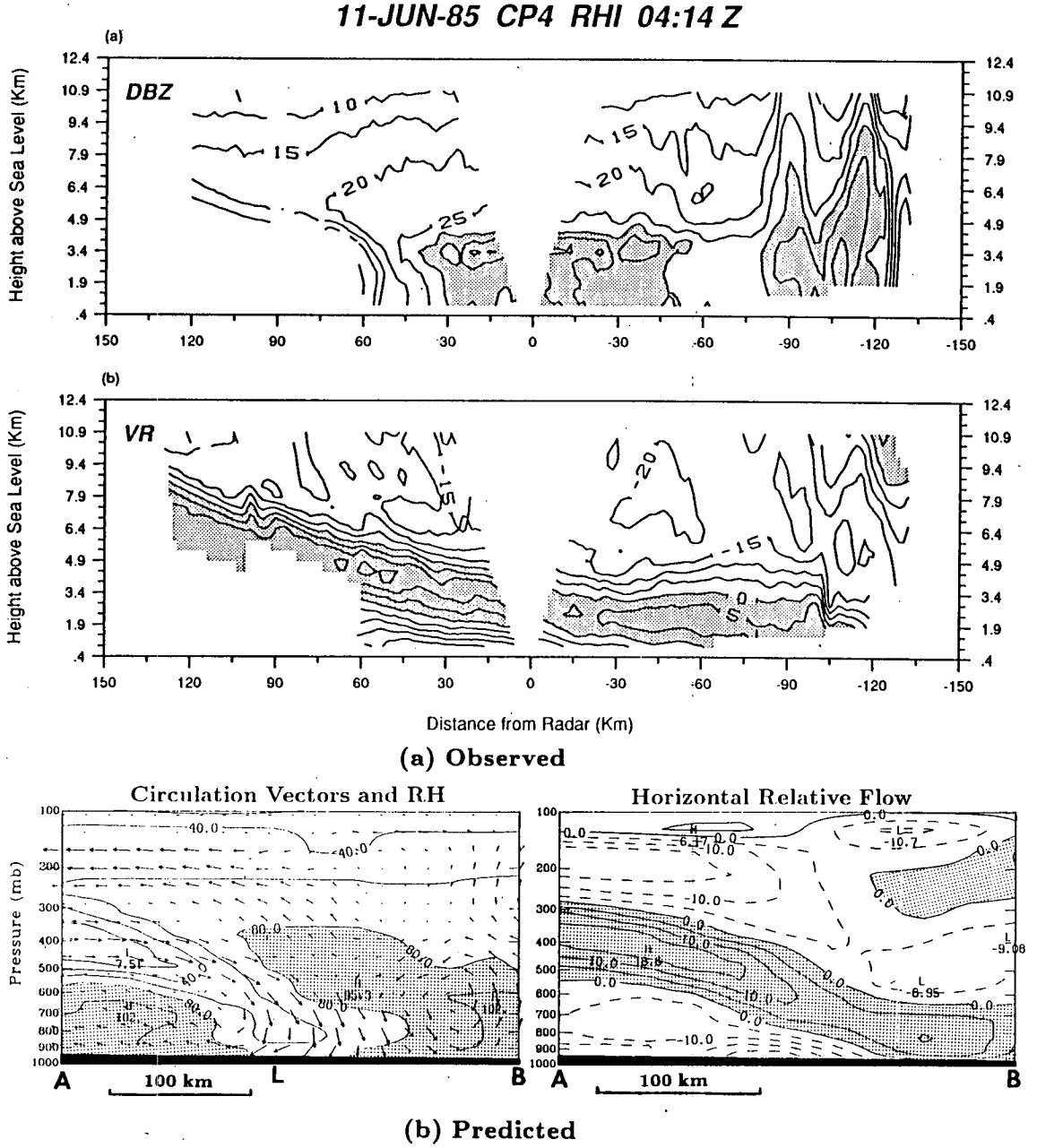

FIG. 22. Vertical cross-sectional comparison of (a) the R88 reflectivity analysis in DBZ (shading denotes reflectivities ≥ 30 DBZ) and horizontal relative flow (along the plane) in m s^{-1} (shading denotes rear-to-front flow) for 0414 UTC 11 June to (b) the simulated relative circulation vectors combined with relative humidity (%), and horizontal relative flow (shading denotes rear-to-front flow) along line *AB* in Fig. 16 from 18-h simulation, verified at 0600 UTC 11 June.

surface isobars). Dramatic increases in rainfall precede the arrival of the wind gust and pressure jump, suggesting that downdraft cooling by evaporation of rainwater is a prominent factor in producing the often observed gust winds and pressure jumps (Fujita 1959, 1985). (Note that the simulated time sequence in which heavy rainfall precedes the wind gust disagrees with the corresponding observations due to the use of the relatively low grid resolutions.) In fact, as the simulated rainfall rate decreases (more likely indicating the approach of the resolvable scale rainfall), the wind gust quickly drops to less than 1.5 m s^{-1} within 45 min. After the passage of the mesohigh, the simulated surface pressure rapidly decreases and reaches a minimum in the wake low with an approximate pressure fall of 6 mb within 1½ h. Associated with the arrival of the wake low are the termination of the rainfall and another strong ageostrophic wind gust. As can be seen from Figs. 15 and 16, this wind actually shifts from northwesterly associated with the mesohigh to northeasterly associated with the wake low with a diffluent axis between. It is important to point out that the model handled this abrupt pressure change quite well and did not show an increase in the area-averaged noise level or any unphysical instability.

At 0900 UTC 11 June (i.e., 21 h into the simulation), both the observed and simulated squall lines diminished, and had mostly propagated out of the network. As showed by JH88, the wake low tended to split into two parts around 0500 UTC. The model appears to reproduce this scenario reasonably well (Fig. 18). At 1200 UTC 11 June, the entire squall system moved out of the fine-mesh domain; only the position of the simulated 500 mb trough axis is shown in Fig. 3 for the reader's information.

c. *Simulations of the vertical and midtropospheric structure*

For the present case, JH88, R88 and Augustine and Zipser (1987) documented well various meso-β scale dynamic and thermodynamic structures associated with a rear-inflow jet and stratiform rainfall. Thus, this provides a great opportunity for the test of the model's performance in reproducing those features from the conventional-data-produced initial conditions.

Before making more detailed comparisons between observations and the simulations, let us first take a look at the lower-level (850 mb) distribution of vertical motion (ω, μb s^{-1}) and relative vorticity (10^{-5} s^{-1}) associated with the squall line from the 18-h simulation (see Fig. 19). A SW–NE oriented upward-motion band developed in correspondence to the leading deep convective line, whereas a band of mesoscale descending motion was produced beneath the upper-level stratiform cloud with the maximum sinking associated with the wake low. The descending motion below the stratiform region was much stronger than the squall-related

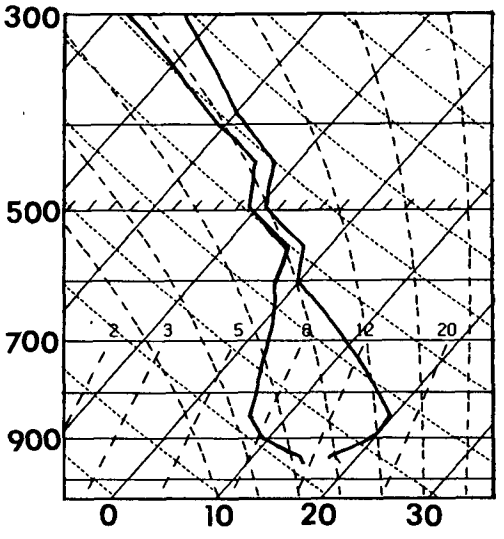

FIG. 23. Simulated "onion-shaped" sounding taken within the wake low.

ascending motion, indicating that the mesoscale downdrafts are thermodynamically generated rather than formed by the compensating subsidence from mesoscale ascent or the leading upward motion. Note the generation of another small area of favorable upward motion behind the wake low that appears to be analogous to the observed weak convective cells over that region (see Fig. 3 in R88). The major features in the simulated vorticity field are cyclonic vorticity associated with the leading squall line and anticyclonic vorticity associated with the mesoscale downdrafts; they are basically controlled by the distribution of divergence and convergence. As will be shown in the next subsection, the presence of the maximum vorticity over southeastern Kansas is a result of a propagating mesovortex.

One of the most encouraging results from this simulation is that the model reproduced the rear-inflow jet associated with the squall system as evident through comparisons against high-resolution-time-sequence windprofiler data. It is worth noting that in the 90-minute-resolution rawinsonde data, the rear-inflow jet is only marginally discernable (see Fig. 6 in Augustine and Zipser 1987). Figures 20 and 21 compare the observed profiler winds (adapted from Augustine and Zipser 1987) to the simulated wind profiles as a function of time for McPherson, Kansas, and Liberal, Oklahoma. Note that to show the steady-state nature of the jet distant from the squall system, the simulated wind profiles have been extended over a much larger time interval than in the Augustine–Zipser analysis. The magnitude and vertical distribution, timing and location, and upward tilting with time of the simulated rear-inflow agree remarkably well with the observed structure, although the model appears to underpredict the strength of the rear-inflow jet at Liberal by 2–5 m

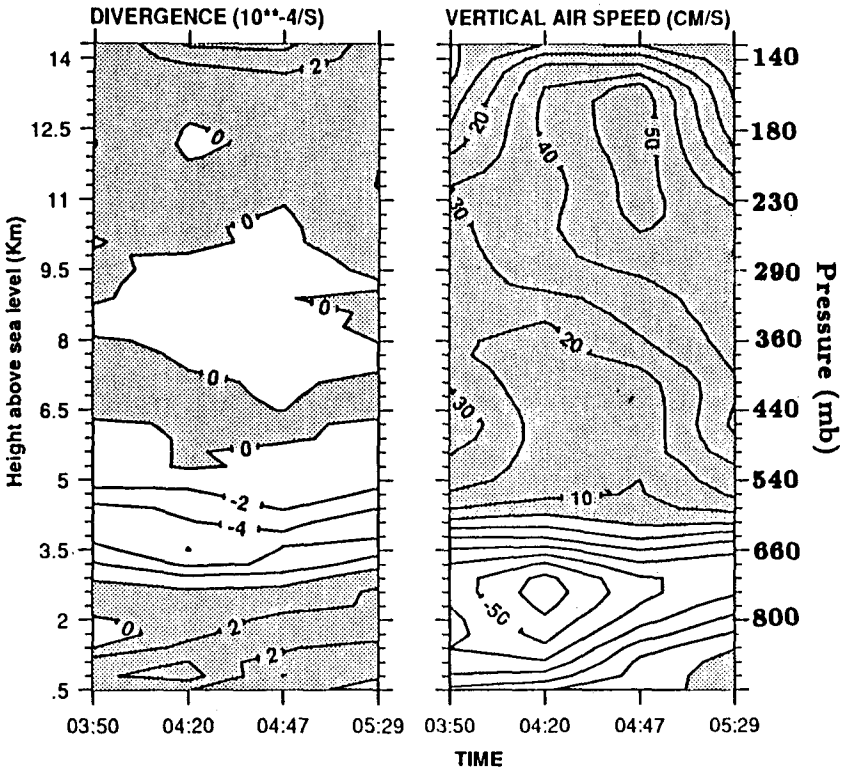

(a) Observed

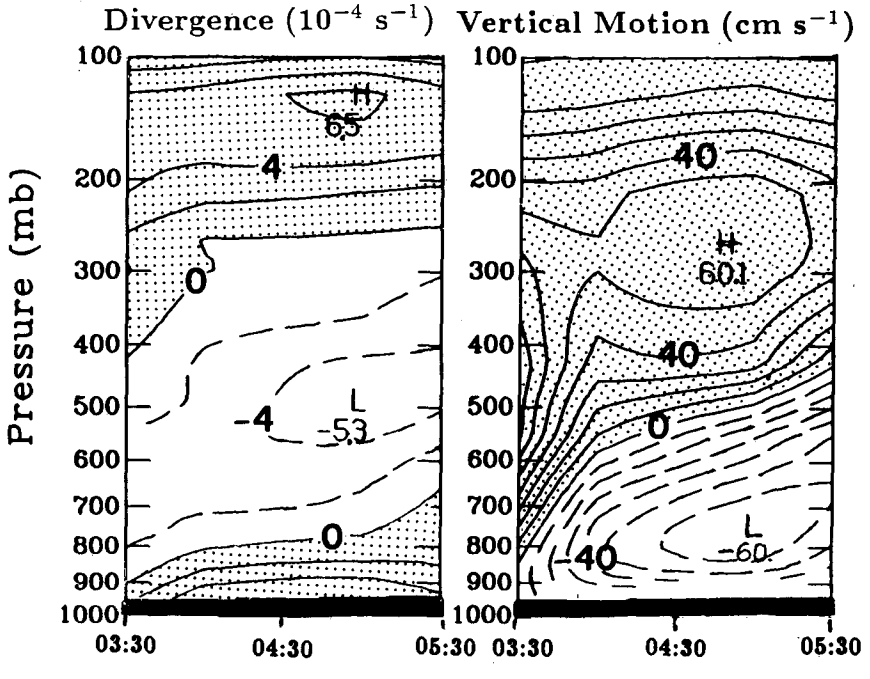

(b) Predicted

FIG. 24. Comparison of (a) the EVAD (extended velocity-azimuth display) derived time evolution of divergence and vertical motion from R88 to (b) the simulated at the location *C* in Fig. 16.

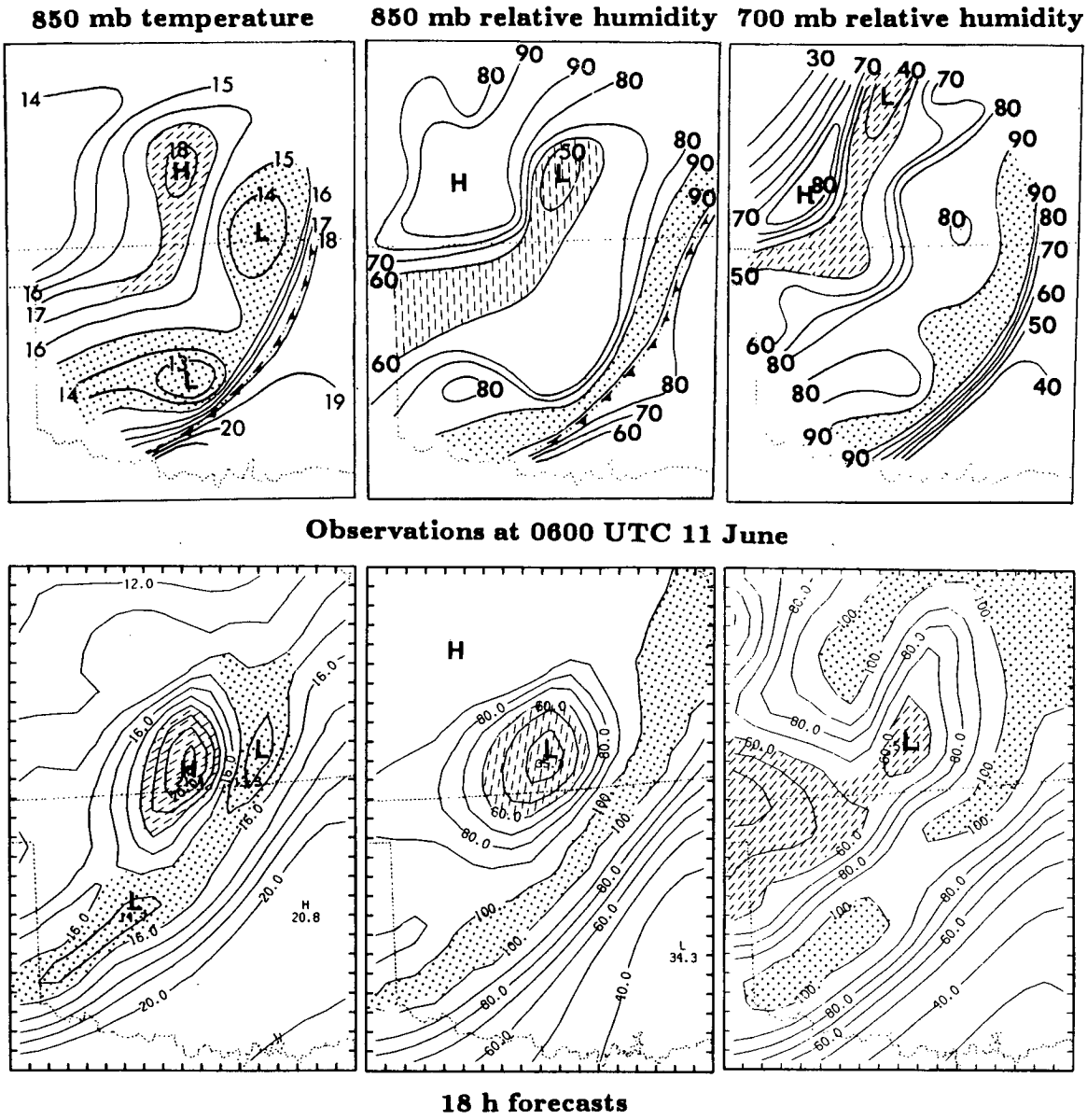

FIG. 25. Comparison of the observed 850 mb temperature (left panel) and relative humidity (middle panel), and 700 mb relative humidity (right panel) reproduced from JH88 to the 18-h simulated, verified at 0600 UTC 11 June. Shading indicates cold and moist region behind the leading line and hatching indicates warm and dry region associated with the surface wake low.

s^{-1} around 7 km during the period 0300–0500 UTC 11 June. The simulated wind profiles below 3 km for McPherson also conform to that derived from Doppler-acoustic-sounder data (see Fig. 5 in Augustine and Zipser 1987), particularly for indicating the passage of the surface front, the strong low-level veering wind profiles ahead of the squall line and backing wind profiles behind the line. The model also reproduces the basic structure of the wind profiles at profiler sites of Denver, Platteville, Fleming and Flagler in Colorado (not shown). Note that windprofilers often fail to provide wind measurements in the convective region, and sometimes produce anomalous information due to the use of the consensus-averaging algorithm, as pointed out by Augustine and Zipser (1987). Hence, in this regard, numerical models can become a very useful tool in filling gaps in windprofiler data for the purpose of certain diagnostic computations. On the other hand, the excellent agreement between the simulated wind structure and the high-resolution windprofiler data greatly improves the credibility of the model simulation, as well as diagnostic and scientific sensitivity studies to be presented in forthcoming papers.

Figure 22 compares the vertical cross-sectional anal-

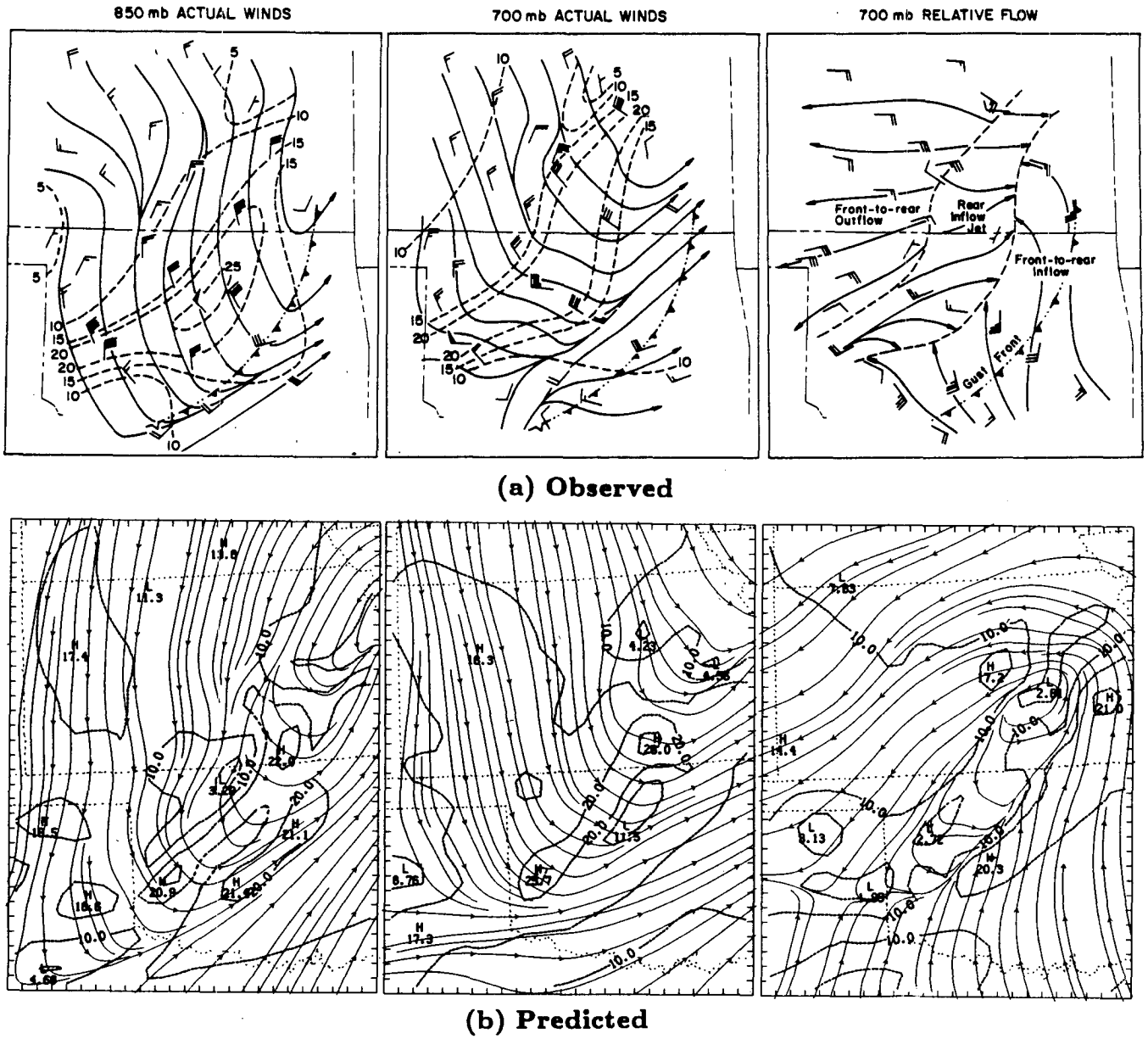

FIG. 26. Comparison of composited 850 mb actual flow (left panel), 700 mb actual flow (central panel) and 700 mb relative flow (right panel) reproduced from JH88 to the 18-h simulated, verified at 0600 UTC 11 June. Dashed lines are isotaches in m s^{-1}.

ysis of the simulated relative humidity (RH) and relative circulation vectors to the R88 radar reflectivity analysis, and the simulated horizontal relative flow to that estimated from their single-Doppler data, both at an equivalent scale. Note that ice saturation was not considered in producing Fig. 22b (but was included in the model computation). Thus, 5%–10% underestimation of relative humidity (w.r.t. ice) can be expected above 600 mb level. As shown in Fig. 22, the model reproduces fairly well the observed precipitation distribution. The simulated convective region is characterized by stronger upward motion, followed by descent and weak vertical motion to the left. This reduction in vertical motion appears to be responsible for the generation of the observed transition zone with relatively weak radar returns. This will be discussed in Part II. Farther to the left (rear), the observed rearward tilt of the radar echo and trailing stratiform clouds are well represented by the simulated vertical motion and RH pattern. A vertical sounding (Fig. 23) taken within the wake low shows a well-known "onion-shaped" structure (see Zipser 1969, 1977; Johnson 1986; Leary and Rappaport 1987). It should be pointed out that the simulation shows marginally saturated conditions

above the 0°C isotherm. Thus, the underestimation of relative humidity above 600 mb in Fig. 23 is again due to the neglect of ice saturation. From Figs. 22 and 23, it becomes evident that the low-level warming and drying can be directly attributed to mesoscale unsaturated downdrafts associated with subsidence within the rear-to-front flow, and the wake low is hydrostatically generated by the adiabatic warming of this descending air. JH88 also found "onion-shaped" soundings near the wake low in the 10–11 June squall line. Another result evident in Fig. 22 is that the model reproduced rather well the cross-sectional distribution of the flow structure, namely, two front-to-rear relative flows at respective lower and upper levels with the rear-inflow jet between. In particular, both the horizontal and vertical scales, and vertical orientation of the simulated rear-inflow jet compare favorably to the observed.

Figure 24 compares the time–height cross section of the EVAD (extended velocity-azimuth display) derived divergence and vertical motion (cm s^{-1}) behind the leading line from R88 to the simulated. The simulated cross section was taken at a point close to CP-3 radar site (see Fig. 16 for the location) and roughly through the lateral dimension of the squall system. The simulated structures and magnitudes resemble closely the EVAD-derived distribution. Moreover, the simulated structures are similar to that typically observed in other midlatitude (see Figs. 15–18 in Ogura and Liou 1980) and tropical (see Figs. 15 and 16 in Gamache and Houze 1982) squall lines. Familiar features are the relatively strong upward motion (w in cm s^{-1}) associated with convective region, a rapid decrease in w-velocity above the transition zone and then an increase in w-velocity in the stratiform region. As the system passed by, the axes of maximum convergence as well as vanishing upward motion tilt rearward with height. This tilting appears to correspond to the vertical orientation of the descending rear-inflow jet. The stratiform region is characterized by an extensive area of mesoscale downdrafts overlaid by mesoscale upward motion. The midlevel concentrated mass convergence ($\leq -50 \times 10^{-5}$ s^{-1}) feeds both mesoscale updrafts and downdrafts, causing the maximum sinking (≤ -60 cm s^{-1}) at 800 mb, an intense ascending (≥ 60 cm s^{-1}) at 300 mb and strong divergence ($\geq 65 \times 10^{-5}$ s^{-1}) near the tropopause. Some differences between the simulation and EVAD-derived distribution are also evident, but they may be attributed to the space offset of the squall lines, and different methods used to obtain the time–height cross sections and errors in the EVAD-derived values (the error range is within 10%–20%, Matejka, personal communication 1988).

To further show the model's performance in reproducing the distribution of tropospheric thermal and wind fields, Figs. 25 and 26 compare the pressure-surface analyses of the observed temperature, relative humidity and horizontal winds at 850 and 700 mb again to the 18-h simulation. The basic structure of observations and forecasts are quite similar. Relatively warm and dry air is present ahead of the squall line, resulting partly from presquall compensating subsidence and partly from horizontal advection by larger-scale flow. A cold and nearly saturated belt is located within the stratiform region with a strong thermal gradient across the leading convective line. Although this cold, moist belt lags behind the upward motion associated with the leading convective portion (cf. Figs. 19 and 25), the

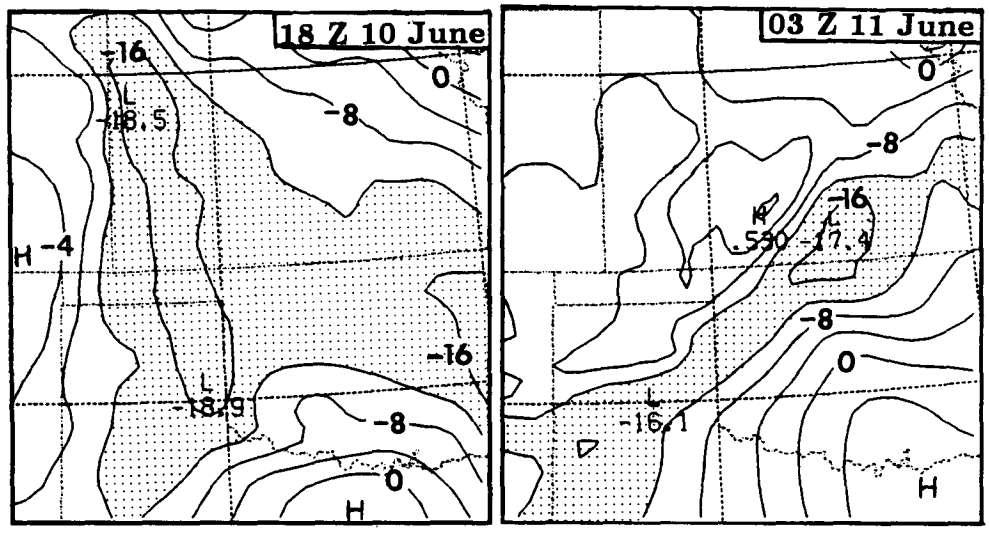

FIG. 27. Distribution of ($\theta_{es500} - \theta_{e850}$) index at interval of 4°K from (a) 6-h and (b) 15-h simulations, verified at 1800 UTC 10 and 0300 UTC 11 June. The term θ_{es500} is the saturated equivalent potential temperature at 500 mb and θ_{e850} is the 850 mb equivalent potential temperature. Shading indicates the values of $\theta_{es500} - \theta_{e850}$ less than −12 K.

parameterized moist downdrafts and adiabatic cooling must have contributed to the generation of such a thermal condition. The evaporation of the resolvable-scale condensates from middle to upper levels appears to have enhanced the cooling and moistening processes. The phase shift between the upward motion and the cool–moist belt seems to be a propagation characteristics of the squall system and similar to that described by Ross and Orlanski (1982) and Orlanski and Ross (1984) for the evolution of an observed cold front. Toward the back edge of the squall system, a drying and warming occurs, hydrostatically leading to the formation of the wake low (cf. Figs. 16, 19 and 25). Note that the maximum warming and drying also lag the maximum sinking, and that the wake low are located at a place where the sinking occurred the longest. From Fig. 22, it is clear that the drying and warming are directly related to the descending rear inflow. More detailed descriptions of the relationship between the rear inflow and wake low will be provided in Part II of this series of papers.

In addition to the simulation of the major squall events, the model, as previously mentioned, produced an observed weak and shallow convective band to the rear of the wake low (see radar analysis in Fig. 16). Specifically, the model simulated well-developed surface convergence (Fig. 16), favorable upward motion up to 600 mb (Figs. 19 and 22b) and a moist band in low troposphere (Figs. 22b and 25) behind the wake low. Clearly, the wake low dynamically contributed to this lower-level destabilization. However, deep convection is not possible over this region because, as shown in Fig. 22b, the tilted descending rear inflow acted as a "lid" preventing any deep convective overturning from occurring.

The simulated low-level flow structure at both 850 and 700 mb also compare favorably to the JH88 composite analysis (Fig. 26). Note that the JH88 composite was obtained by advecting the 0300 and 0900 UTC wind data foreward and backward, respectively, assuming a steady state. Since the squall line was observed to decay very rapidly after 0400 UTC, the JH88 composite tends to overestimate the strongest winds while underestimating the weakest winds. In particular, as will be detailed in the next subsection, both the observations and simulation show the presence of a mesovortex within the northern portion of the squall system. The simulated 700 mb relative flow exhibits a closed cyclonic circulation over eastern Kansas whereas the JH88 composite analysis fails to show this important feature. Nevertheless, both the JH88 analysis and the simulation exhibit troughlike flow characteristics, and the downward slope of the rear-inflow jet. The leading convective line developed along the convergence axis between the northwesterly and southwesterly flow. It is of interest to note from the simulated 700 mb relative flow that the presence of the mesovortex appears to help enhance the strength of the rear-inflow jet, since the position of the rear-inflow jet coincided with the

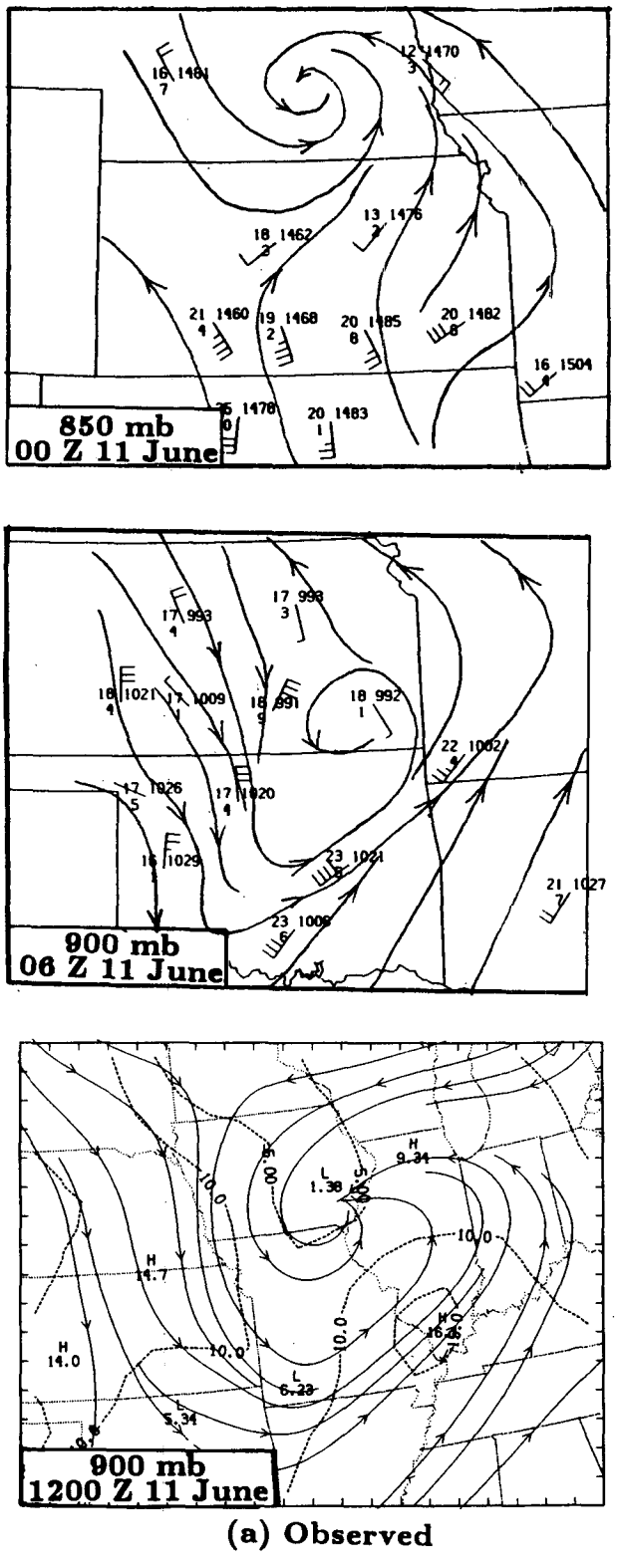

FIG. 28. (a) Observational streamline analyses at 850 mb for 0000 UTC 11 June and at 900 mb for 0600 and 1200 UTC 11 June. A full barb is 5 m s^{-1}. The 1200 UTC frame is produced using only the standard network data and in a subdomain of the coarse mesh. (b) The σ-level (=0.873) streamline analyses from the simulation for the time indicated. The dashed lines are isotachs in m s^{-1}.

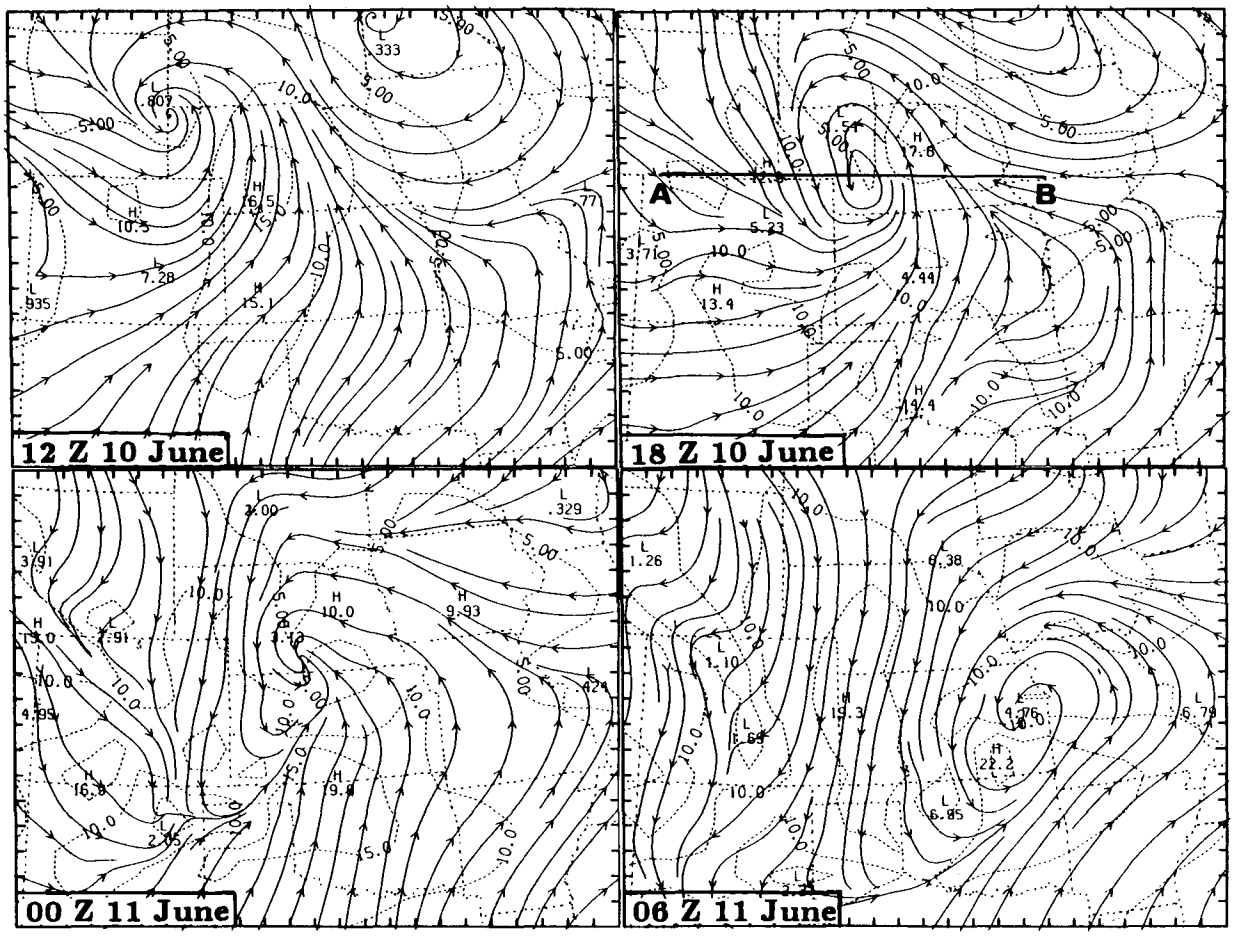

(b) Predicted

FIG. 28. (*Continued*)

southern rear-to-front stream lines of the mesovortex. In this sense, the present squall line has three-dimensional structure, as also shown by the horizontal distribution of vertical motion and vorticity in Fig. 19. Smull and Houze (1985) and Leary and Rappaport (1987) also found the correspondence of rear inflow to a midlevel cyclonic circulation centered within the stratiform region.

As previously mentioned, both the observed and simulated squall lines intensified rapidly as they advanced into the network, then dissipated rapidly as they moved out of the network. JH88 speculated, based upon a theoretical modeling study by Rotunno et al. (1988), that this resulted from the transformation of environments from a favorable low-level wind shear interacting with the extensive cool pool to a less favorable wind shear condition. Although such an environmental transformation was well simulated in this model (see Figs. 20 and 21), we felt that the following mechanism was basically operative. Figure 27a,b shows the distribution of the simulated $(\theta_{es500} - \theta_{e850})$ index about 2–3 h prior to the occurrence of the rapid intensification and dissipation, respectively. The variable θ_{es500} is the saturated equivalent potential temperature at 500 mb whereas θ_{e850} is the 850 mb equivalent potential temperature. The $(\theta_{es500} - \theta_{e850})$ index is similar to the lifted index concept in which lower index values denote a more conditionally unstable environment. It is evident that the rapid evolution of the squall line is strongly associated with the horizontal variation of stability over the Oklahoma–Kansas area. Hence, the presence of the less favorable wind shear condition could not be used here to explain the rapid dissipation of the system after 0300 UTC. Note that a north–south oriented band of the minimum $(\theta_{es500} - \theta_{e850})$ (i.e., ≤ -16°K) at 1800 UTC that corresponds to the convergence line associated with the warm front (see Figs. 7 and 8). The model squall line was initiated as the sector *A* front interacted with this unstable band of the minimum $(\theta_{es500} - \theta_{e850})$. This widespread conditionally unstable mass is more likely a consequence of the interaction between the first convective system and the

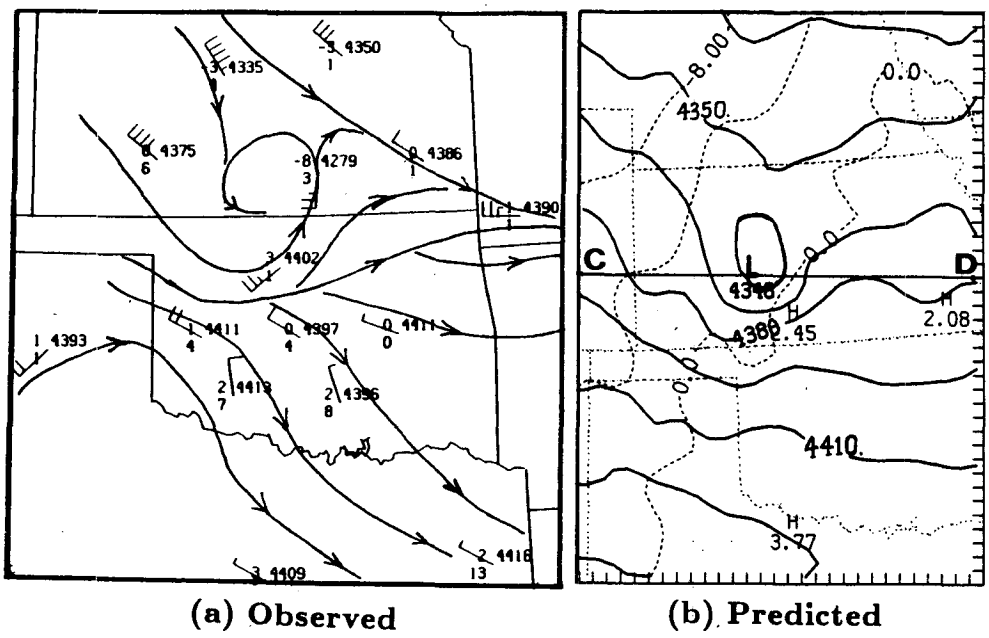

FIG. 29. Comparison of (a) 600 mb observations at 0300 UTC 11 June to (b) the distribution of the 15-h simulated 600 mb height (solid lines) at intervals of 15 m and temperature (dashed lines) at intervals of 4°C.

daytime mixed-layer development. Specifically, the dissipated first system tends to moisten the low- to midtroposphere while the daytime heating helps eliminate the initial surface inversion and weaken the cool pool produced by the first system, thereby generating convectively favorable conditions for the development of deep convection. In fact, like the 1977 Johnstown squall line (Zhang and Fritsch 1988a), when the ground temperature was held constant in time, the model fails to produce the 10–11 June squall line (not shown). During the nighttime hours, the longwave radiation tends to cool the boundary layer, making air parcels less able to tap the potential buoyant energy. Of course, strong lifting from the parameterized downdrafts may have also contributed to the evolution of the squall system. When the parameterized downdrafts in the Fritsch–Chappell scheme were omitted, the model produced more than a 3-h delay of the squall

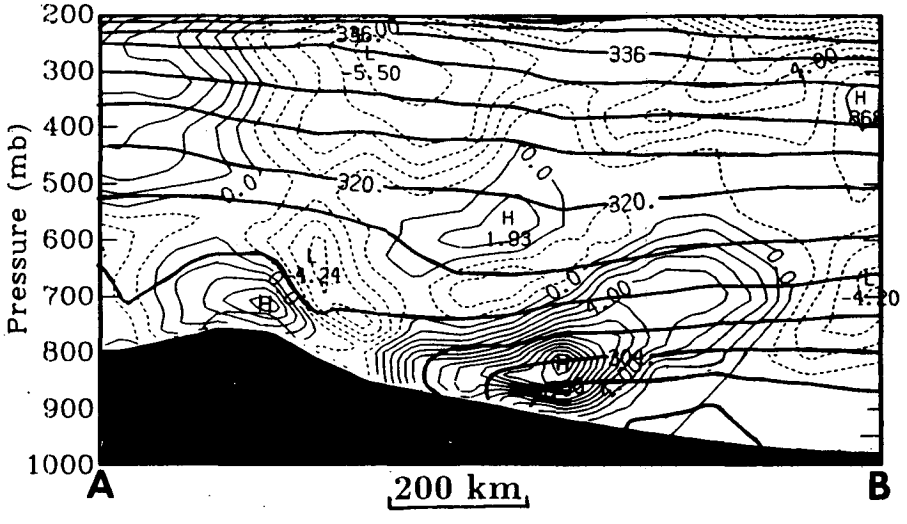

FIG. 30. West–east vertical cross section of the potential temperature (thick solid lines) at intervals of 4 K and relative vorticity (other lines) at intervals of 10^{-5} s^{-1} through the vortex center along line AB in Fig. 28b from 6-h simulation, verified at 1800 UTC 10 June. The thin solid lines denote a positive vorticity and dashed lines denote a negative vorticity.

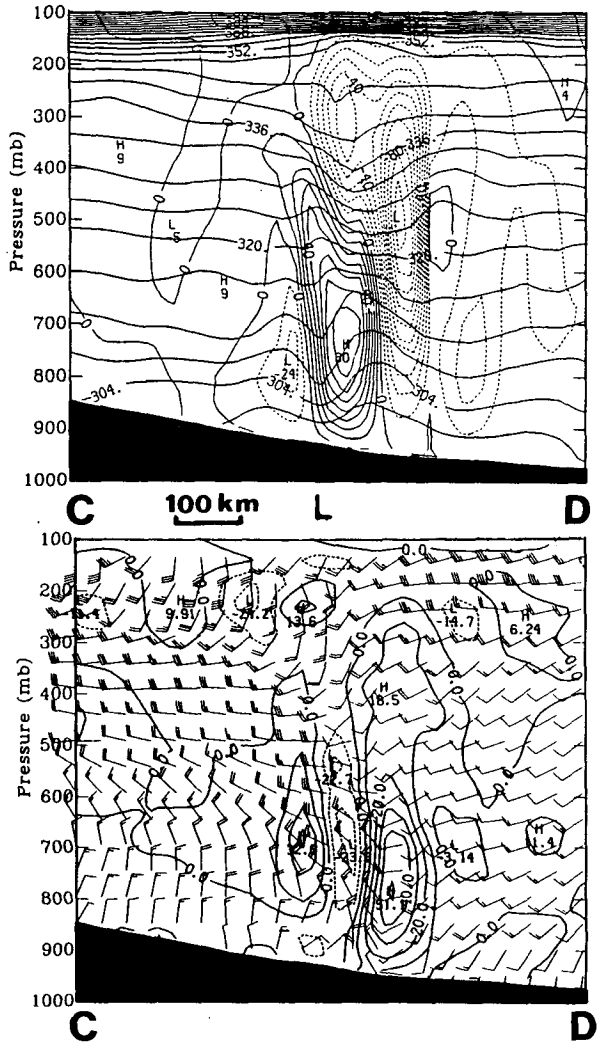

FIG. 31. West–east vertical cross section of (a) potential temperature (solid lines) at intervals of 4 K and ω at intervals of 10 μb s^{-1} (dashed lines denote upward motion); and (b) horizontal winds (direction is common convention, a full barb is 10 m s^{-1}) and relative vorticity (solid lines are positive and dashed lines are negative) at intervals of 10^{-4} s^{-1} from 15-h simulation, verified at 0300 UTC 11 June along line CD in Fig. 29.

line formation in time and space, and significant reduction in its intensity (not shown). All of these sensitivity studies will be presented in a forthcoming paper.

d. Simulation of a mesovortex

Many different studies of MCSs show that significant stratiform precipitation is well correlated with the appearence and intensification of mesovortices (Houze 1977; Leary and Rappaport 1987; Zhang and Fritsch 1987, 1988b). As mentioned earlier, a mesovortex was also observed to occur in the present case; it is most apparent between 0300 and 1200 UTC 11 June (see Figs. 28a and 29a). The model simulates quite well the location, flow structure, and strength of the vortex. At 0300 UTC when the squall system was in its strongest stage, a closed mesolow near 600 mb developed in both observations and the simulation (Fig. 29). It is found that 600 mb is about the level where the best-defined mesolow was located. Above 600 mb, its magnitude tends to decrease as a result of the net warming by latent heat release. However, it is extremely important to point out that the present mesovortex was not generated by latent heat release associated with the squall system but formed prior to the model initial time.

Figure 28b shows the 18-h evolution of the simulated mesovortex starting from the model initial time. Initially, the vortex was centered at the borders of Wyoming, Nebraska and South Dakota, slightly behind the frontal low. It exhibits a circulation on a meso-α scale, which is distinct from the latent-heating generated meso-β scale vortices (see Johnston 1981; Johnson 1986; Zhang and Fritsch 1987). (Investigation of how this vortex was formed is beyond the scope of this study.) Like the squall line, its propagation seems to be linked to the evolution of 700 mb short-wave trough where the maximum geostrophic vorticity was presumably located, and differs from the movement of the frontal (presquall) low. By 1200 UTC 11 June, the vortex center has moved near the Iowa–Illinois borders, and according to JH88, later appears to have contributed to surface cyclogenesis over Ohio Valley. To examine the evolution of the vortex's vertical structure, west–east vertical cross sections through the vortex center before (i.e., 1800 UTC 10 June) and after (0300 UTC 11 June) the development of the squall system are presented in Figs. 30 and 31, respectively. At the beginning, a strong cyclonic vorticity associated with the vortex concentrates only within the lowest 100 mb. (This is the reason why the simulated stream line analyses in Fig. 28b are presented at the σ = 0.873 level.) One of the particularly interesting questions here is how this shallow vortex could be well preserved over the first 12-h period in which the latent heating contributed little to the maintenance of cyclonic vorticity against frictional dissipation, Ekman spindown (the *e*-folding time is about 1 day) and absorption by the larger-scale flow. With the aid of the nonlinear inertial stability argument (Schubert and Hack 1982), it can be understood that strong cyclonic rotation of horizontal winds tends to generate resistance to radial displacement of air parcels such that a mesovortex once formed will not quickly decay. Furthermore, based on the potential vorticity conservation principle (Holton 1979, p. 89), the southeastward and downslope movement of the vortex tends to acquire more cyclonic vorticity from a decrease in the Coriolis parameter and an increase in the thickness of low-level constant θ surfaces. Of course, the presence of geostrophic vorticity associated with the short-wave could further help the maintenance of the vortex.

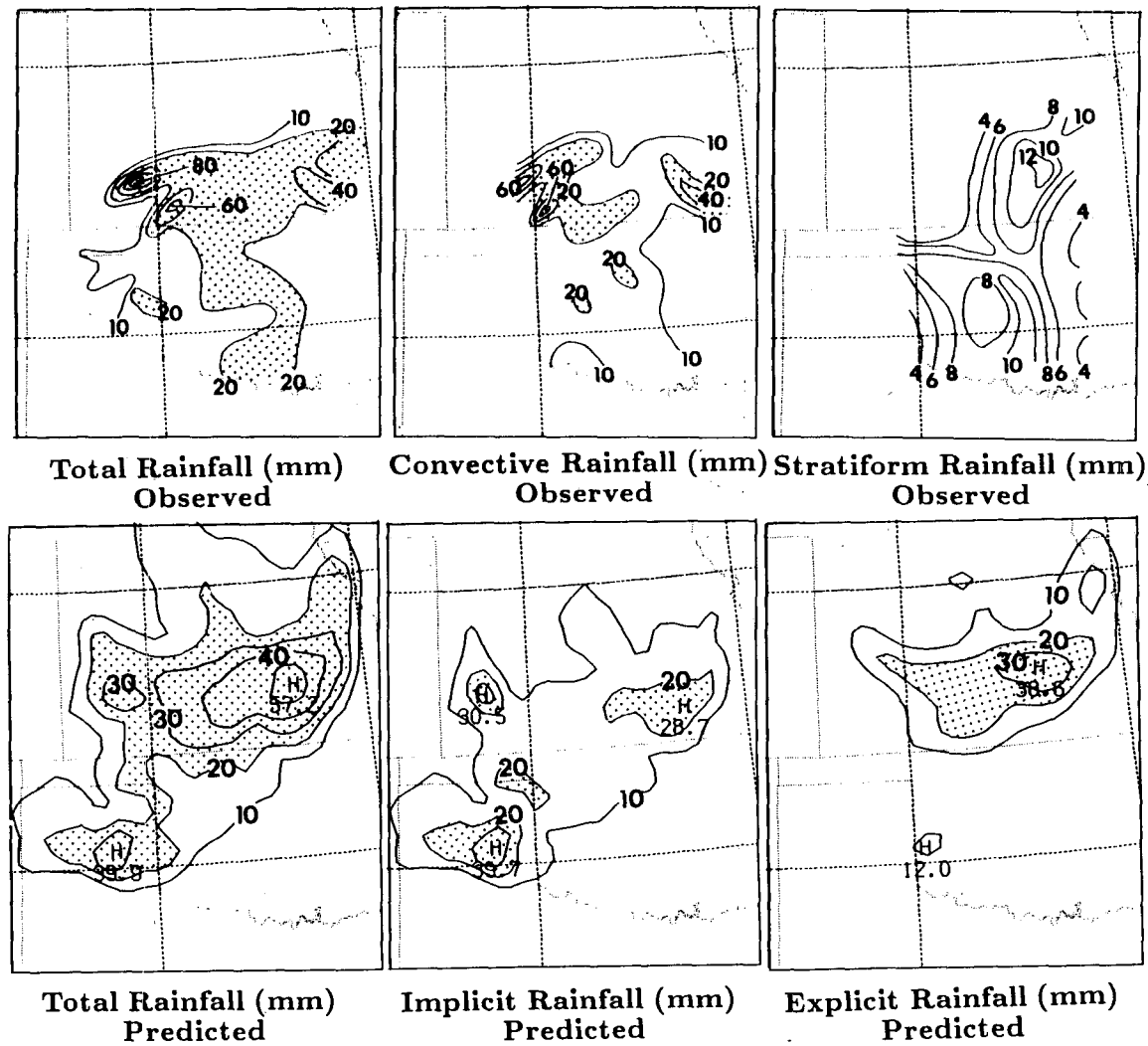

FIG. 32. Comparison of the observed total, convective and stratiform rainfall (upper row, reproduced from JH88) to the simulated (lower row). Rainfall greater than 20 mm is shaded. The rainfall associated with the first convective system has been excluded in the calculation.

While the latent heating associated with the squall system was not responsible for the generation of the mesovortex, it assisted the intensification and vertical stretching of cyclonic vorticity into a much deeper layer (see Fig. 31). Note though that the maximum relative vorticity (51×10^{-5} s^{-1}) still occurs in the low troposphere. Associated with the vortex is a strong upward motion with its maximum (ω, -90 μb s^{-1}) near 500 mb. Other relevant features in Fig. 31 include: (i) larger amplitude of warm-core structure within upper-tropospheric stratiform region; (ii) the coldest pool occurred some distance below 600 mb, indicating possible importance of the ice melting and evaporation; (iii) the mesoscale sinking associated with the rear-inflow jet took place beneath the trailing stratiform cloud with its maximum behind and below the coldest pool; (iv) strong convergence of horizontal winds along the interface between the rear-to-front and front-to-rear relative flow; (v) vertically coherent, troughlike winds developed up to 600 mb where a changeover to rearward tilted structure occurred; and (vi) if a relative-flow pattern is constructed from Fig. 31b, a front-to-rear inflow ahead of the squall system and a rear-to-front inflow behind are clearly apparent up to 300 mb with divergent outflow near the tropopause. Although it is difficult to verify these simulated structures for the present squall line, the results conform to many other case studies for tropical and midlatitude MCSs (e.g., Houze 1977; Ogura and Liou 1980).

e. Simulation of convective and stratiform rainfall

Precipitation is an important end product of a model simulation, and the most difficult variable to be verified

against observations, particularly on the meso-β scale. This is because both convective and stratiform rainfall in the model are parameterized, although differently, with limited knowledge in relation to resolvable-scale variables. Nevertheless, it is still important to compare the present simulation to the high-resolution network-provided rainfall data in order to gain insight into the role of different model physics in producing rainfall. As has already been shown in Figs. 12, 15 and 16, hourly rainfall rates compare reasonably well to the R88 radar composite. The resolvable-scale rainfall occurred to the rear of the squall line as observed. Fig. 32 compares the simulated convective, stratiform and total rainfall (between 2100 UTC 10 June and 0900 UTC 11 June) associated with the squall line to the observational analysis by JH88. Note that the stratiform rainfall in the observations was empirically determined whenever hourly rainfall rates were less than 6 mm h^{-1}. This partitioning differs from that of the model rainfall. If the JH88 criterion was used to partition the model rainfall, part of the resolvable-scale rainfall can be considered as (mesoscale) convective, which would bring the relative intensities and contributions of these two components into closer agreement with the observations.

The rainfall comparisons between forecasts and observations are generally favorable, particularly for convective portions. For instance, the local maximum convective amounts during the initiation phase over the western region, the relatively uniform convective rainfall during the mature phase over the central region and another convective rainfall maximum to the east during the dissipating phase are well simulated. The amounts are all slightly less than the observed but this may be due to the different rainfall partitioning procedure. Evidence for this conclusion is suggested by the simulated resolvable-scale rainfall over the central-eastern region being larger than the observed. It is also possible that the stratiform rainfall maximum in reality may fall out of the network area, since the JH88 analyzed maximum in Fig. 32 is close to the eastern network boundary. Nonetheless, the location and orientation of the simulated maximum stratiform rainfall resemble the observed, and are consistent with the distribution of the radar reflectivity which showed an intensification of the stratiform precipitation over this region. Satellite imagery also showed a colder cloud top around 0300 UTC (Fig. 6) within the stratiform region, more likely corresponding to the location of the mesovortex, since both the simulation and observations indicated intense stratiform rainfall over that region. Thus, the intense stratiform rainfall may be a result of interaction between stratiform condensation and the mesovortex (see Zhang and Fritsch 1987, 1988b for a detailed discussion). Specifically, the mesovortex provided favorable organized mesoscale ascent to help low-level air parcels reach condensation whereas

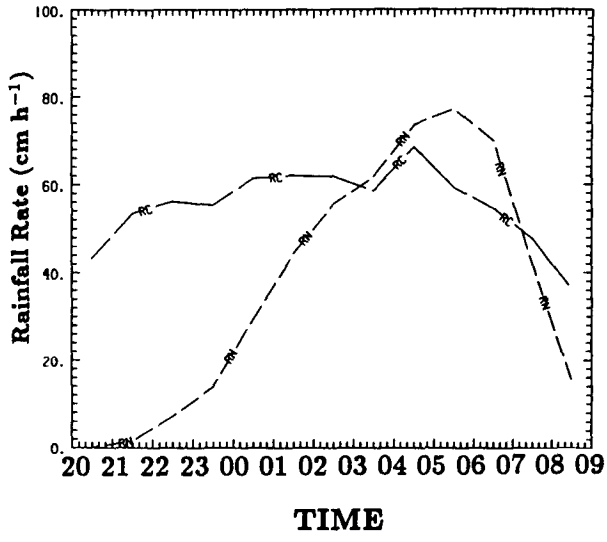

FIG. 33. The time evolution (2000 UTC 10–0900 UTC 11 June) of the grid-box accumulated hourly convective (RC) and resolvable-scale (RN) rainfall rate (cm h^{-1}) for the simulated squall system.

the resulting latent heat release facilitated the intensification and stretching of the vortex. Note another maximum stratiform rainfall center over western Oklahoma which developed in the simulation due to the splitting of the wake low. This maximum is slightly too far to the west of the observed feature.

Figure 33 shows the grid-box accumulated hourly rainfall rate associated with the squall line as a function of time. Since the overpredicted (Colorado) portion of the squall line started to produce convective rainfall before the major squall line formed, the accumulated convective rainfall rate is a little too large at 2000 UTC. The convective rainfall rate exhibits a general trend of an increase up to 0430 UTC and then a decrease afterwards, corresponding fairly well to the evolution of the squall line. The squall area-averaged rainfall rate is about 4–5 mm h^{-1}. However, this trend is much smaller than the resolvable-scale counterpart. In particular, the simulated stratiform rainfall rate between 0300 and 0700 UTC exceeds the convective portion, and the timing of its decay lags 1 h behind the convective rate. To a certain extent this is in agreement with the satellite and radar sequences which showed the peak intensity of convective cells at 0300 UTC and an extensive area of stratiform rainfall thereafter. Furthermore, the simulated relatively uniform convective rainfall rate and the rapid variation in the stratiform rainfall rate conform to the observations if the observed convective and stratiform rainfall were accumulated, respectively, along the squall isochrones shown in Fig. 13. It can be estimated from Fig. 33 that the resolvable-scale rainfall accounts for roughly 40% of the rainfall totals, which is slightly larger than the JH88 analysis.

5. Summary and concluding remarks

In this paper, a 24-h nested-grid simulation of an intense squall line that occurred during 10–11 June 1985 PRE-STORM has been presented. A modified version of the PSU/NCAR three-dimensional mesoscale hydrostatic model was utilized in which implicit convective parameterization schemes and explicit moisture package are simultaneously incorporated. The model was initialized at 1200 UTC 10 June with the standard rawinsonde observations, and integrated with a fine-mesh grid increment of 25 km. The model reproduced quite well a MCS over the network area and an elongated convective system along a cold front over the northwest portion of the fine-mesh domain during the first couple of hours. In particular, the model simulated the initiation of the major squall line along the surface front at nearly the right time, approximately 50–60 km behind the observed position. Comparisons of the simulation with observational analyses of Johnson and Hamilton (1988), Rutledge et al. (1988), Augustine and Zipser (1987), Vasiloff and Bluestein (1988) and other available data showed remarkable capabilities of the present model in reproducing much of the observed meso-β scale structure and evolution up to 24 h. These include (i) the development of several convective bands at 2100 UTC; (ii) the rapid intensification and rapid dissipation processes of the squall line as it entered into and moved out of the network area, respectively; (iii) the generation of a presquall mesolow, a squall-induced mesohigh and a wake low as well as corresponding multiple surface convergence–divergence flows; (iv) the evolution of a traveling 700 mb shortwave; (v) the development of a rear-inflow jet; (vi) the leading convective rainfall followed by a transition zone and trailing stratiform precipitation; (vii) the vertical relative flow configuration of the rear-to-front inflow jet overlaid by a front-to-rear flow with a low-level front-to-rear outflow to the rear of the squall system; (viii) the simulation of "onion-shaped" soundings; (ix) the splitting of the wake low; (x) the maintenance and intensification of a mesovortex; (xi) the distribution and magnitude of convective and stratiform rainfall; and (xii) the diurnal cycle of the planetary boundary layer.

It is found that the squall line was initiated as a surface front moved into a convectively unstable environment (i.e., interacted with a thermal boundary). The rapid evolution of the squall line most likely resulted from variations in the convective environment into which the system was propagating. The interaction of the low-level wind shear with the convectively generated cool pool provides an additional mechanism for explaining the initial rapid intensification process. The wake low was a persistent feature with a lifetime more than 50% of the squall line and was found to be hydrostatically generated by the descending rear-inflow jet. The "onion-shaped" soundings were shown to be the low- to midlevel manifestation of the surface wake low. A discussion of the mechanisms whereby the wake low forms and its impact on the evolution of the squall system will be presented in Part II of this series of papers. It has been shown that the present mesovortex was not generated by latent heat release associated with the squall system but rather was present prior to the model initial time. During the mature stage of the squall system, the mesovortex appears to have contributed to the generation of the organized stratiform rainfall, and enhanced the intensity of the rear-inflow jet. On the other hand, the latent heating assisted the vertical stretching and intensification of the vortex. A large portion of the stratiform rainfall could be related to the presence of the mesovortex.

Based upon the present simulation and previously published numerical case studies by Zhang and Fritsch (1986, 1988b), we may state that the meso-β scale structure and evolution of MCSs under certain synoptic environmental conditions can be well predicted using the standard network data if compatible grid resolution, reasonable model physics and initial conditions are utilized. The results indicate that the convective and boundary-layer parameterization schemes and the explicit moisture physics in this model are realistic for being utilized to study the meso-β scale structure and evolution of MCSs.

Acknowledgments. We are grateful to B. Smull, R. Rotunno, and an anonymous reviewer for their constructive comments that helped improve an earlier version of this paper. We benefited from discussions with J. Augustine, G. Barnes, D. Blanchard, J. Cunning, Y. R. Guo, R. Johnson, J. Klemp, M. LeMone, T. Matejka, M. Moncrieff, and E. Zipser. We thank the Mesoscale and Microscale Meteorology Division, NCAR for the computer support during the course of this study. The computations were performed at the NCAR CRAY X-MP.

REFERENCES

Anthes, R. A., and T. T. Warner, 1978: Development of hydrostatic models suitable for air pollution and other mesometeorology studies. *Mon. Wea. Rev.*, **106**, 1045–1078.

——, E.-Y. Hsie and Y.-H. Kuo, 1987: Description of the Penn State/NCAR mesoscale model version 4 (MM4). NCAR Tech. Note, NCAR/TN-282, 66pp.

Augustine, J. A., and E. J. Zipser, 1987: The use of wind profilers in a mesoscale experiment. *Bull. Amer. Meteor. Soc.*, **68**, 4–17.

Benjamin, S. G., and N. L. Seaman, 1985: A simple scheme for improved objective analysis in curved flow. *Mon. Wea. Rev.*, **113**, 1184–1198.

——, and T. N. Carlson, 1986: Some effects of surface heating and topography on the regional severe storm environment. Part I: Three-dimensional simulation. *Mon. Wea. Rev.*, **114**, 307–329.

Carlson, T. N., and F. H. Ludlam, 1968: Conditions for the occurrence of severe local storms. *Tellus*, **20**, 203–226.

Chang, C. B., D. J. Perkey and C. W. Kreitzberg, 1981: A numerical

case study of the squall line of 6 May 1975. *J. Atmos. Sci.*, **38**, 1601–1615.

Cho, H.-R., and D. S. Chan, 1987: Mesoscale atmospheric dynamics and modeling of rainfall fields. *J. Geophys. Res.*, **92**, 9687–9692.

Cunning, J. B., 1986: The Oklahoma–Kansas Preliminary Regional Experiment for STORM-Central. *Bull. Amer. Meteor. Soc.*, **67**, 1478–1486.

——, and D. O. Blanchard, 1987: Mesoscale interactions in the development of a large squall line system. *Extended Abstracts, Third Conference on Mesoscale Processes*, Vancouver, Amer. Meteor. Soc., 36.

Delsol, F., K. Miyakoda and R. H. Clarke, 1971: Parameterized processes in the surface boundary layer of an atmospheric circulation model. *Quart. J. Roy. Meteor. Soc.*, **97**, 181–208.

Fritsch, J. M., and C. F. Chappell, 1980: Numerical prediction of convectively driven mesoscale pressure systems. Part I: Convective parameterization. *J. Atmos. Sci.*, **37**, 1722–1733.

——, R. A. Maddox and A. G. Barnston, 1981: The character of mesoscale convective complex precipitation and its contribution to warm season rainfall in the U. S. Preprints, *Fourth Conference on Hydrometeorology*, Reno, Amer. Meteor. Soc., 94–99.

Fujita, T. T., 1959: Precipitation and cold air production in mesoscale thunderstorm systems. *J. Meteor.*, **16**, 454–466.

——, 1963: *Analytical Mesometeorology. A Review. Met. Monogr.*, No. 5, 77–125.

——, 1985: The downburst. Rep. of Projs. NIMROD and JAWS, The University of Chicago, 122 pp.

Gamache, J. F., and R. A. Houze, Jr., 1982: Mesoscale air motions associated with a tropical squall line. *Mon. Wea. Rev.*, **110**, 118–135.

Geogakakos, K. P., and M. D. Hudlow, 1984: Quantitative precipitation forecast techniques for use in hydrologic forecasting. *Bull. Amer. Meteor. Soc.*, **65**, 1186–1200.

Heideman, K. F., and J. M. Fritsch, 1988: Forcing mechanisms and other characteristics of significant summertime precipitation. *Wea. Forecasting*, **3**, 115–130.

Holton, J. R., 1979: *An Introduction to Dynamic Meteorology*. Academic Press, 391 pp.

Hoskins, B. J., E. C. Neto and H.-R. Cho, 1984: The formation of multiple fronts. *Quart. J. Roy. Meteor. Soc.*, **110**, 881–896.

Houze, R. A., Jr., 1977: Structure and dynamics of a tropical squall–line system. *Mon. Wea. Rev.*, **105**, 1540–1567.

Hsie, E.-Y., R. A. Anthes and D. Keyser, 1984: Numerical simulation of frontogenesis in a moist atmosphere. *J. Atmos. Sci.*, **41**, 2581–2594.

Johnson, R. H., 1986: The development of organized mesoscale circulation within Oklahoma–Kansas PRE–STORM convective system. Preprints, *Int. Conf. on Monsoon and Mesoscale Meteorology*, Taiwan, 100–104.

——, and P. J. Hamilton, 1988: The relationship of surface pressure features to the precipitation and air flow structure of an intense midlatitude squall line. *Mon. Wea. Rev.*, **116**, 1444–1472.

Johnston, E. C., 1981: Mesoscale vorticity centers induced by mesoscale convective complexes. M. S. thesis, Dept. of Meteor., University of Wisconsin, 54 pp.

Kalb, M. W., 1987: The role of convective parameterization in the simulation of a Gulf coast precipitation system. *Mon. Wea. Rev.*, **115**, 214–234.

Leary, C. A., and R. A. Houze, Jr., 1979: Melting and evaporation of hydrometers in precipitation from anvil clouds of deep tropical convection. *J. Atmos. Sci.*, **36**, 669–679.

——, and E. N. Rappaport, 1987: The life cycle and internal structure of a mesoscale convective complex. *Mon. Wea. Rev.*, **115**, 1503–1527.

Lin, Y.-L., R. D. Farley and H. D. Orville, 1983: Bulk parameterization of the snow field in a cloud model. *J. Climate Appl. Meteor.*, **22**, 1065–1092.

Maddox, R. A., 1980: Mesoscale convective complexes. *Bull. Amer. Meteor. Soc.*, **61**, 1374–1387.

——, L. R. Hoxit and C. F. Chappell, 1980: A study of tornadic thunderstorm interactions with thermal boundaries. *Mon. Wea. Rev.*, **108**, 322–336.

Molinari, J., and M. Dudek, 1986: Implicit versus explicit convective heating in numerical weather prediction models. *Mon. Wea. Rev.*, **114**, 1822–1831.

Moncrieff, M. W., and M. J. Miller, 1976: The dynamics and simulation of tropical squall line. *Quart. J. Roy. Meteor. Soc.*, **102**, 373–394.

Newton, C. W., 1950: Structure and mechanism of the prefrontal squall line. *J. Meteor.*, **7**, 210–222.

——, 1967: Severe convective storms. *Advances in Geophysics*, Vol. 12, Academic Press, 257–303.

Ogura, Y., and M. T. Liou, 1980: The structure of a midlatitude squall line: A case study. *J. Atmos. Sci.*, **37**, 553–567.

Orlanski, I., and B. B. Ross, 1984: The evolution of an observed cold front. Part II: Mesoscale dynamics. *J. Atmos. Sci.*, **41**, 1669–1703.

Pedgley, D. E., 1962: A meso–synoptic analysis of the thunderstorms on 28 August 1958. Brit. Meteor. Off., Geophys. Mem. No. 106, 74 pp.

Perkey, D. J., and C. W. Kreitzberg, 1976: A time-dependent lateral boundary scheme for limited-area primitive equation models. *Mon. Wea. Rev.*, **104**, 744–755.

Purdom, J. F., 1976: Some uses of high–resolution GOES imagery in the mesoscale forecasting of convection and its behavior. *Mon. Wea. Rev.*, **104**, 1474–1483.

Ramage, C. S., 1982: Have precipitation forecasts improved? *Bull. Amer. Meteor. Soc.*, **63**, 739–743.

Ross, B. B., 1987: The role of low-level convergence and latent heating in a simulation of observed squall line formation. *Mon. Wea. Rev.*, **115**, 2298–2321.

——, and I. Orlanski, 1982: The evolution of an observed cold front. Part I: Numerical simulation. *J. Atmos. Sci.*, **39**, 296–327.

Rotunno, R., J. B. Klemp and M. L. Weisman, 1988: A theory for strong, long–lived squall line. *J. Atmos. Sci.*, **45**, 463–485.

Rutledge, S. A., and P. V. Hobbs, 1983: The mesoscale and microscale structure and organization of clouds and precipitation in midlatitude cyclones. VIII: A model for the "seeder–feeder" process in warm-frontal rainbands. *J. Atmos. Sci.*, **40**, 1185–1206.

——, and D. R. MacGorman, 1988: Cloud-to-ground lightning activity in the 10–11 June 1985 mesoscale convection system observed during Oklahoma–Kansas PRE–STORM project. *Mon. Wea. Rev.*, **116**, 1393–1408.

——, R. A. Houze, Jr., M. I. Biggerstaff and T. Matejka, 1988: The Oklahoma–Kansas mesoscale convective system of 10–11 June 1985: Precipitation structure and single-Doppler radar analysis. *Mon. Wea. Rev.*, **116**, 1409–1430.

Schubert, W. H., and J. J. Hack, 1982: Inertial stability and tropical cyclone development. *J. Atmos. Sci.*, **39**, 1687–1697.

Seaman, N. L., D. R. Stauffer and T. T. Warner, 1988: Effects of forecasts of mesoscale meteorological structures caused by grid nesting in a three-dimensional numerical model. Preprints, *Eighth Conf. on Numerical Weather Prediction*, Amer. Meteor. Soc., J67–74.

Smull, B. F., and R. A. Houze, Jr., 1985: A midlatitude squall line with a trailing region of stratiform rain: Radar and satellite observations. *Mon. Wea. Rev.*, **113**, 117–133.

——, and ——, 1987a: Dual–Doppler radar analysis of a midlatitude squall line with a trailing region of stratiform rain. *J. Atmos. Sci.*, **44**, 2128–2148.

——, and ——, 1987b: Rear-inflow in squall lines with trailing stratiform precipitation. *Mon. Wea. Rev.*, **115**, 2869–2889.

Uccellini, L. W., and D. R. Johnson, 1979: The coupling of upper and lower tropospheric jet streaks and implications for the development of severe convective storms. *Mon. Wea. Rev.*, **107**, 682–703.

Vasiloff, S. V., and H. B. Bluestein, 1988: Analysis of the Oklahoma segment of the 10–11 June 1985 severe squall line: Maturity to

decay. Preprints, *15th Conf. on Severe Local Storms,* Baltimore, Amer. Meteor. Soc., 288–291.

Zehnder, J. A., and P. R. Bannon, 1988: Frontogenesis over a mountain ridge. *J. Atmos. Sci.,* **45,** 628–644.

Zhang, D.-L., 1989: The effect of parameterized ice microphysics on the simulation of vortex circulation with a mesoscale hydrostatic model. *Tellus,* **41A,** 132–147.

——, and R. A. Anthes, 1982: A high-resolution model of the planetary boundary layer–sensitivity tests and comparisions with SESAME-79 data. *J. Appl. Meteor.,* **21,** 1594–1609.

——, and J. M. Fritsch, 1986: Numerical simulation of the meso-β scale structure and evolution of the 1977 Johnstown flood. Part I: Model description and verification. *J. Atmos. Sci.,* **43,** 1913–1943.

——, and ——, 1987: Numerical simulation of the meso-β scale structure and evolution of the 1977 Johnstown flood. Part II: Inertially stable warm-core vortex and the mesoscale convective complex. *J. Atmos. Sci.,* **44,** 2593–2612.

——, and ——, 1988a: Numerical sensitivity experiments of varying model physics on the structure, evolution and dynamics of two mesoscale convective systems. *J. Atmos. Sci.,* **45,** 261–293.

——, and ——, 1988b: A numerical investigation of a convectively generated, inertially stable, extratropical warm-core mesovortex over land. Part I: Structure and evolution. *Mon. Wea. Rev.,* **116,** 2660–2687.

——, H.-R. Chang, N. L. Seaman, T. T. Warner and J. M. Fritsch, 1986: A two-way interactive nesting procedure with variable terrain resolution. *Mon. Wea. Rev.,* **114,** 1330–1339.

——, E.-Y. Hsie and M. W. Moncrieff, 1988: A comparison of explicit and implicit predictions of convective and stratiform precipitating weather systems with a meso-β scale numerical model. *Quart. J. Roy. Meteor. Soc.,* **114,** 31–60.

Zipser, E. J., 1969: The role of organized unsaturated downdrafts in the structure and rapid decay of an equatorial disturbance. *J. Appl. Meteor.,* **8,** 799–814.

——, 1977: Mesoscale and convective-scale downdrafts as distinct components of squall-line circulation. *Mon. Wea. Rev.,* **105,** 1568–1589.